

Chapter 9

Simulations of Wave Propagation in Metamaterials

In this chapter, we present some interesting simulations of wave propagation in metamaterials. We start in Sect. 9.1 with a perfectly matched layer model, which allows us to reduce the simulation on an infinite domain to be realized on a bounded domain. Here we present a simulation demonstrating the negative refraction index phenomenon for metamaterials. In Sects. 9.2 and 9.3, we present invisibility cloak simulations using metamaterials in frequency domain and time domain, respectively. In Sect. 9.4, we present an interesting application of metamaterials for solar cell design. In Sect. 9.5, we end this chapter by presenting some open mathematical problems related to metamaterials.

9.1 Interesting Phenomena of Wave Propagation in Metamaterials

9.1.1 Demonstration of a PML Model

First, we want to demonstrate the role of a perfectly matched layer (PML) model developed by Ziolkowski [310] in 1999 (see Chap. 8). Following the notation of [310], we assume that the PML is a cubical domain. The complete PML governing equations on the corner region are given by (cf. Sect. 8.2.4):

$$\frac{\partial \mathbf{E}}{\partial t} + D_1 \mathbf{E} = \frac{1}{\epsilon_0} \nabla \times \mathbf{H} - \frac{1}{\epsilon_0} \mathbf{J}, \quad (9.1)$$

$$\frac{\partial \mathbf{J}}{\partial t} + D_2 \mathbf{J} = \epsilon_0 D_3 \mathbf{E}, \quad (9.2)$$

$$\frac{\partial \mathbf{H}}{\partial t} + D_1 \mathbf{H} = -\frac{1}{\mu_0} \nabla \times \mathbf{E} - \frac{1}{\mu_0} \mathbf{K}, \quad (9.3)$$

$$\frac{\partial \mathbf{K}}{\partial t} + D_2 \mathbf{K} = \mu_0 D_3 \mathbf{H}. \quad (9.4)$$

Recall that the 3×3 diagonal matrices

$$D_1 = \text{diag}(\sigma_y + \sigma_z - \sigma_x, \sigma_z + \sigma_x - \sigma_y, \sigma_x + \sigma_y - \sigma_z),$$

$$D_2 = \text{diag}(\sigma_x, \sigma_y, \sigma_z),$$

$$D_3 = \text{diag}((\sigma_x - \sigma_y)(\sigma_x - \sigma_z), (\sigma_y - \sigma_x)(\sigma_y - \sigma_z), (\sigma_z - \sigma_x)(\sigma_z - \sigma_y)),$$

where σ_x, σ_y and σ_z are nonnegative functions and represent the damping variations along the x, y and z directions, respectively. Usually, quadratic profiles are chosen for σ_x, σ_y and σ_z [284, 310].

Note that the model (9.1)–(9.4) is the same as (5.12) of Turkel and Yefet [284] (assuming $\epsilon_0 = \mu_0 = 1$) and is well-posed mathematically because it is a symmetric hyperbolic system plus lower order terms [284, p. 545].

Since the PML model (9.1)–(9.4) is very similar to the metamaterial Drude model solved by the nodal discontinuous Galerkin method discussed in Sect. 4.4, we can easily solve the PML model (9.1)–(9.4) by the nodal discontinuous Galerkin method. Details can be found in the original paper [185].

For simplicity, here we just solve a 2-D transverse magnetic PML model, which can be obtained from (9.1) to (9.4):

$$\frac{\partial H_x}{\partial t} = -\frac{\partial E_z}{\partial y} - K_x + (\sigma_x - \sigma_y)H_x, \quad (9.5)$$

$$\frac{\partial H_y}{\partial t} = \frac{\partial E_z}{\partial x} - K_y - (\sigma_x - \sigma_y)H_y, \quad (9.6)$$

$$\frac{\partial E_z}{\partial t} = \frac{\partial H_y}{\partial x} - \frac{\partial H_x}{\partial y} - J_z - (\sigma_x + \sigma_y)E_z, \quad (9.7)$$

$$\frac{\partial J_z}{\partial t} = \sigma_x \sigma_y E_z, \quad (9.8)$$

$$\frac{\partial K_x}{\partial t} = -\sigma_x K_x + (\sigma_x - \sigma_y)\sigma_x H_x, \quad (9.9)$$

$$\frac{\partial K_y}{\partial t} = -\sigma_y K_y - (\sigma_x - \sigma_y)\sigma_y H_y, \quad (9.10)$$

where the subscripts ‘ x, y ’ and ‘ z ’ denote the corresponding components.

For this 2-D PML model, we assume that the physical domain $\Omega = (-1, 1)^2$ is surrounded by a perfectly matching layer of thickness of 0.2, which makes the real computational domain $(-1.2, 1.2)^2$. The initial electric source is given as

$$E_z(x, y, 0) = \begin{cases} \cos^6(\frac{\pi r}{2r_0}) & \text{if } r \leq r_0 \\ 0 & \text{if } r \geq r_0 \end{cases} \quad (9.11)$$

where $r_0 = 0.5$, $r = \sqrt{x^2 + y^2}$. Furthermore, the damping function σ_x is chosen as:

$$\sigma_x(x) = \begin{cases} \sigma_0(x-1)^2 & \text{if } x \geq 1 \\ \sigma_0(x+1)^2 & \text{if } x \leq -1 \\ 0 & \text{elsewhere,} \end{cases}$$

where σ_0 is a damping constant. The damping function σ_y can be similarly defined using y variable.

Here we present a test result obtained with time step $\tau = 10^{-3}$, damping constant $\sigma_0 = 1$, discontinuous quadratic basis function on a triangular mesh with 2,748 vertices and 5,317 elements, and the simulation time $t \in (0, 1,500 \tau)$ such that the wave front has propagated out of the simulation domain when $t = 1,500 \tau$.

Some snapshots at various time steps are presented in Fig. 9.1, which shows that the PML performs very well since there is no wave reflected back at the interfaces between the PML layer and the free space.

9.1.2 The Multiscale Phenomena for Metamaterials

Here we solve a coupled model problem on a complex domain where a circle $(x - 0.5)^2 + y^2 = 0.5^2$ is located inside a rectangle $[-1.5, 1.5]^2$. The circle region is occupied by a Drude type metamaterial, which is governed by the non-dimensionalized 2-D transverse magnetic metamaterial modeling equations (4.59)–(4.64) with sources $g_x = g_y = f = 0$, i.e.,

$$\begin{aligned} \frac{\partial H_x}{\partial t} &= -\frac{\partial E_z}{\partial y} - K_x, \\ \frac{\partial H_y}{\partial t} &= \frac{\partial E_z}{\partial x} - K_y, \\ \frac{\partial E_z}{\partial t} &= \frac{\partial H_y}{\partial x} - \frac{\partial H_x}{\partial y} - J_z, \\ \frac{\partial J_z}{\partial t} &= \omega_e^2 E_z - \Gamma_e J_z, \\ \frac{\partial K_x}{\partial t} &= \omega_m^2 H_x - \Gamma_m K_x, \\ \frac{\partial K_y}{\partial t} &= \omega_m^2 H_y - \Gamma_m K_y. \end{aligned}$$

Outside of the circle but within the rectangle $[-1, 1]^2$ is filled by air, which is modeled by the 2-D transverse magnetic modeling equations:

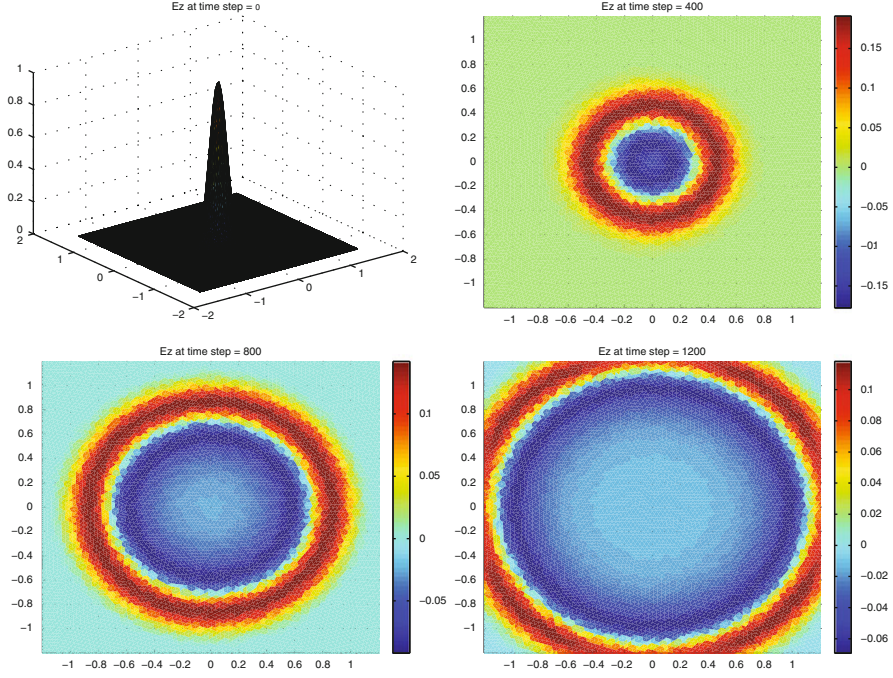


Fig. 9.1 Demonstration of PML effects. (Top Left) Surface plot of E_z at $t = 0$; contour plots of E_z at various time steps: $t = 400\tau$ (Top Right); $t = 800\tau$ (Bottom Left); $t = 1,200\tau$ (Bottom Right)

$$\frac{\partial H_x}{\partial t} = -\frac{\partial E_z}{\partial y} \quad (9.12)$$

$$\frac{\partial H_y}{\partial t} = \frac{\partial E_z}{\partial x} \quad (9.13)$$

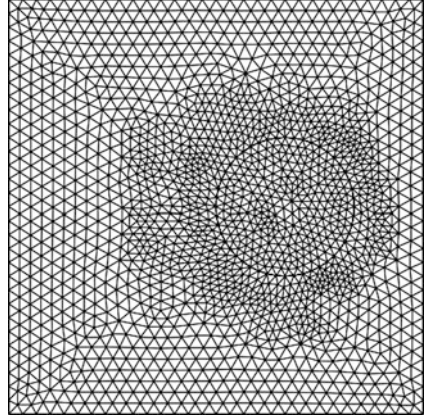
$$\frac{\partial E_z}{\partial t} = \frac{\partial H_y}{\partial x} - \frac{\partial H_x}{\partial y}. \quad (9.14)$$

The remaining area outside of $[-1, 1]^2$ is modeled by the PML equations (9.1)–(9.4).

This coupled model problem is solved by the nodal discontinuous Galerkin method. The initial source wave has the same form as (9.11) but centered at $(-0.5, 0)$. This problem has been solved using various parameters in [185]. After many numerical tests, it is found that the metamaterial model (4.59)–(4.64) has very different wave propagation phenomena, which depend on the relative size of those physical parameters.

Below we present an exemplary result solved with $\Gamma_e = \Gamma_m = 1$, $\tau = 10^{-3}$ on a triangular mesh (see Fig. 9.2) with 1,713 nodes and 3,304 elements. The basis function is second order. The problem is solved with a varying $\omega_e = \omega_m$. Numerical

Fig. 9.2 The mesh and model setup for the coupled problem



results show that when $\omega_e < 1$, the wave can propagate through the metamaterial region without much damage of the initial electric field E_z . When ω_e becomes larger than 1, the wave gets damped as it moves into the metamaterial region. When ω_e is in the range of $[10, 20]$, the wave not only gets damped but also reflects from the metamaterial region. When ω_e is larger than 50, the wave propagates into the metamaterial region and damps very badly without much reflection. The exemplary results shown in Fig. 9.3 are obtained with $\tau = 10^{-3}$ running for 1,000 time steps, and $\omega_e = 0.2, 5, 20, 100$. Figure 9.3 demonstrates again that modeling wave propagation in metamaterials is quite challenging due to the inherited multiscale characteristics.

9.1.3 Demonstration of Backward Wave Propagation

In Sect. 1.1.1, we mentioned that since the refractive index of metamaterial is negative, the phase velocity is antiparallel to the energy flow direction, which fact leads to the so-called backward wave propagation phenomenon in metamaterials.

To demonstrate this phenomenon, Ziolkowski [311] designed some interesting examples to model electromagnetic wave propagation in metamaterials. Following [311], we consider the 2-D transverse magnetic model:

$$\epsilon_0 \frac{\partial E_y}{\partial t} = \frac{\partial H_x}{\partial z} - \frac{\partial H_z}{\partial x} - J_y, \quad (9.15)$$

$$\mu_0 \frac{\partial H_z}{\partial t} = -\frac{\partial E_y}{\partial x} - K_z, \quad (9.16)$$

$$\mu_0 \frac{\partial H_x}{\partial t} = \frac{\partial E_y}{\partial z} - K_x, \quad (9.17)$$

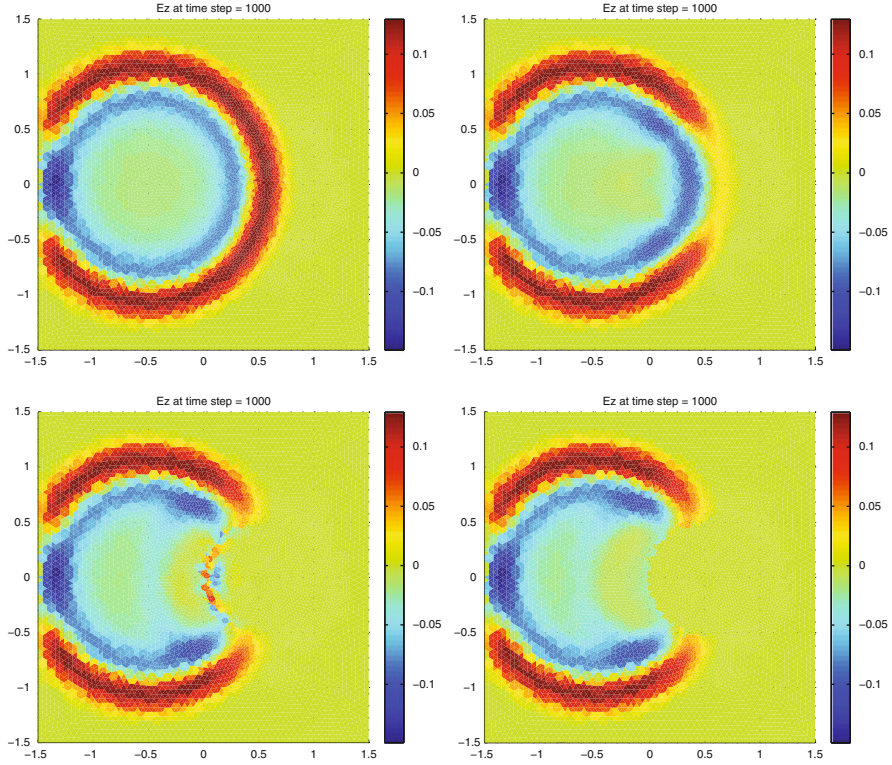


Fig. 9.3 The electric fields obtained with fixed $\Gamma_e = \Gamma_m = 1$, and varying $\omega_e = \omega_m$. (Top Left): $\omega_e = 0.2$; (Top Right): $\omega_e = 5$; (Bottom Left): $\omega_e = 20$; (Bottom Right): $\omega_e = 100$

$$\frac{1}{\epsilon_0 \omega_{pe}^2} \frac{\partial J_y}{\partial t} + \frac{\Gamma_e}{\epsilon_0 \omega_{pe}^2} J_y = E_y, \quad (9.18)$$

$$\frac{1}{\mu_0 \omega_{pm}^2} \frac{\partial K_z}{\partial t} + \frac{\Gamma_m}{\mu_0 \omega_{pm}^2} K_z = H_z, \quad (9.19)$$

$$\frac{1}{\mu_0 \omega_{pm}^2} \frac{\partial K_x}{\partial t} + \frac{\Gamma_m}{\mu_0 \omega_{pm}^2} K_x = H_x, \quad (9.20)$$

where H_z, H_x and E_y are the field components in the z, x and y directions, respectively. Note that this model is obtained using the Drude model introduced in Chap. 1 (cf. (1.12) and (1.13)).

First, we model a normal incidence wave beam interacting with a metamaterial slab with refractive index $n \approx -1$, which can be achieved by choosing

$$\Gamma_e = \Gamma_m = \Gamma = 10^8 \text{ s}^{-1}, \quad \omega_{pe} = \omega_{pm} = \omega_p = 2\pi\sqrt{2}f_0, \quad f_0 = 30\text{GHz}.$$

Note that in this case, the refractive index

$$n(\omega) = \sqrt{\frac{\epsilon(\omega)\mu(\omega)}{\epsilon_0\mu_0}} = 1 - \frac{\omega_p^2}{\omega(\omega - i\Gamma)} \approx -1,$$

where μ_0 and ϵ_0 are the vacuum permeability and permittivity, respectively.

Following Ziolkowski [311], the incident wave is chosen to be varied in space as $\exp(-x^2/\text{waist}^2)$ and in time as

$$f(t) = \begin{cases} 0 & \text{for } t < 0, \\ g_{on}(t) \sin(\omega_0 t) & \text{for } 0 < t < mT_p, \\ \sin(\omega_0 t) & \text{for } mT_p < t < (m+k)T_p, \\ g_{off}(t) \sin(\omega_0 t) & \text{for } (m+k)T_p < t < (2m+k)T_p, \\ 0 & \text{for } (2m+k)T_p < t, \end{cases} \quad (9.21)$$

where we denote $T_p = 1/f_0$, and

$$\begin{aligned} g_{on}(t) &= 10x_{on}^3(t) - 15x_{on}^4(t) + 6x_{on}^5(t), \quad x_{on}(t) = t/mT_p, \\ g_{off}(t) &= 1 - [10x_{off}^3(t) - 15x_{off}^4(t) + 6x_{off}^5(t)], \\ x_{off}(t) &= [t - (m+k)T_p]/mT_p. \end{aligned}$$

In the first example, the simulation domain is chosen as 830×640 cells (z vs. x), where the cell thickness $dx = 10^{-4}$ m. The wave source is located at the center in the x -direction and 40 cells above the bottom of the simulation domain. A metamaterial slab is put at 200 cells above the beam source, and its thickness is 200 cells. The Bérenger PML of eight cells in thickness is used around the simulation domain. The remaining area is modelled by the Maxwell's equations in free space:

$$\begin{aligned} \epsilon_0 \frac{\partial E_y}{\partial t} &= \frac{\partial H_x}{\partial z} - \frac{\partial H_z}{\partial x}, \\ \mu_0 \frac{\partial H_z}{\partial t} &= -\frac{\partial E_y}{\partial x}, \\ \mu_0 \frac{\partial H_x}{\partial t} &= \frac{\partial E_y}{\partial z}, \end{aligned}$$

which can be obtained by choosing $J_y = K_z = K_x = 0$ in (9.15)–(9.20).

The electric field intensity (obtained with time step $dt = 0.1$ ps, the beam waist being 50 cells, and the incident wave (9.21) choosing $m = 2, k = 100$) is plotted in Fig. 9.4, where the left one is the field at 5,000 time steps, which clearly shows that the wave propagates backward inside the metamaterial slab. Another interesting property of metamaterial is that the electromagnetic wave propagates very slowly inside metamaterial. To see this clearly, we plot the electric field

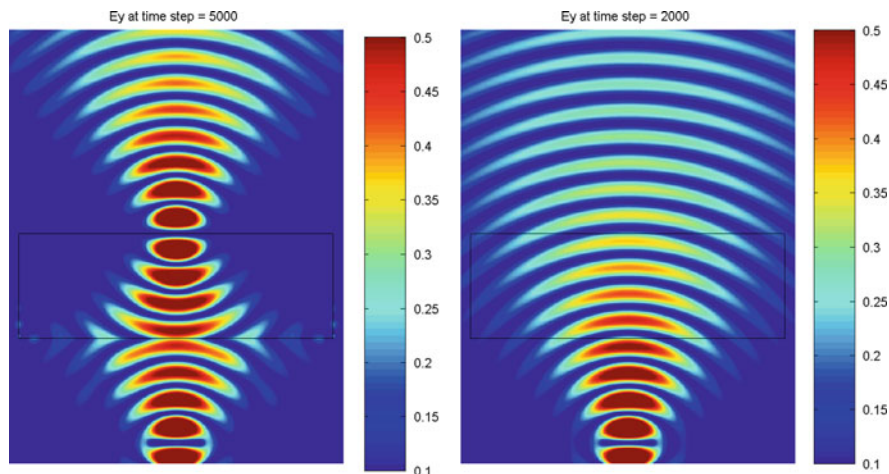


Fig. 9.4 The electric field intensity distribution: (*Left*) passing through a metamaterial slab with $n \approx -1$; (*Right*) passing through free space only (i.e., $n = 1$) (Reprinted from Li et al. [191]. Copyright (2008), with permission from Elsevier)

intensity obtained at 2,000 time steps for a wave propagating in free space (just replacing the metamaterial slab by vacuum) in Fig. 9.4 (Right). This figure shows that the wave reaches the boundary on the other side in only 2,000 time steps, while it takes about 5,000 time steps when a metamaterial slab is present.

Figure 9.4 (Left) also shows that the metamaterial slab has a nice refocusing property, which usually can be achieved by convex lenses. This property has prompted many researchers to work on the so-called perfect lens [234]. Encouraged by this phenomenon, we can further simulate a wave beam interacting with many metamaterial slabs of $n \approx -1$. An example of three slabs is given in [191], where the simulation domain is $1,500 \times 500$ cells (z vs. x), the bottom metamaterial slab is located 240 cells above the bottom side, the distance between each slab is 400 cells. Each slab is 460 cells in width and 200 cells in thickness. The source beam is located at the same place as the previous example. The obtained electric field intensity distribution at different times are presented in Fig. 9.5, which clearly show that the source beam can be transmitted further away via multiple metamaterial slabs. This phenomenon opens the potential applications in nano-waveguides.

The last example modified from [157] is used to demonstrate the backward wave propagation phenomenon and the Snell's law using a triangular metamaterial slab. The physical domain is chosen to be $[0, 0.06] \times [0, 0.064]$ m. The incident source wave is located at $x = 0.004$ m and imposed as a scalar component. A triangle metamaterial slab is determined by vertices (0.014, 0.02), (0.014, 0.062) and (0.044, 0.062). Outside this slab is vacuum. For this example, a hybrid mesh is used, where a triangular mesh is used for the metamaterial slab and its neighboring elements, and a rectangular mesh is used in the vacuum region and PML region. A leap-frog mixed finite element method is used for this example, where the lowest-

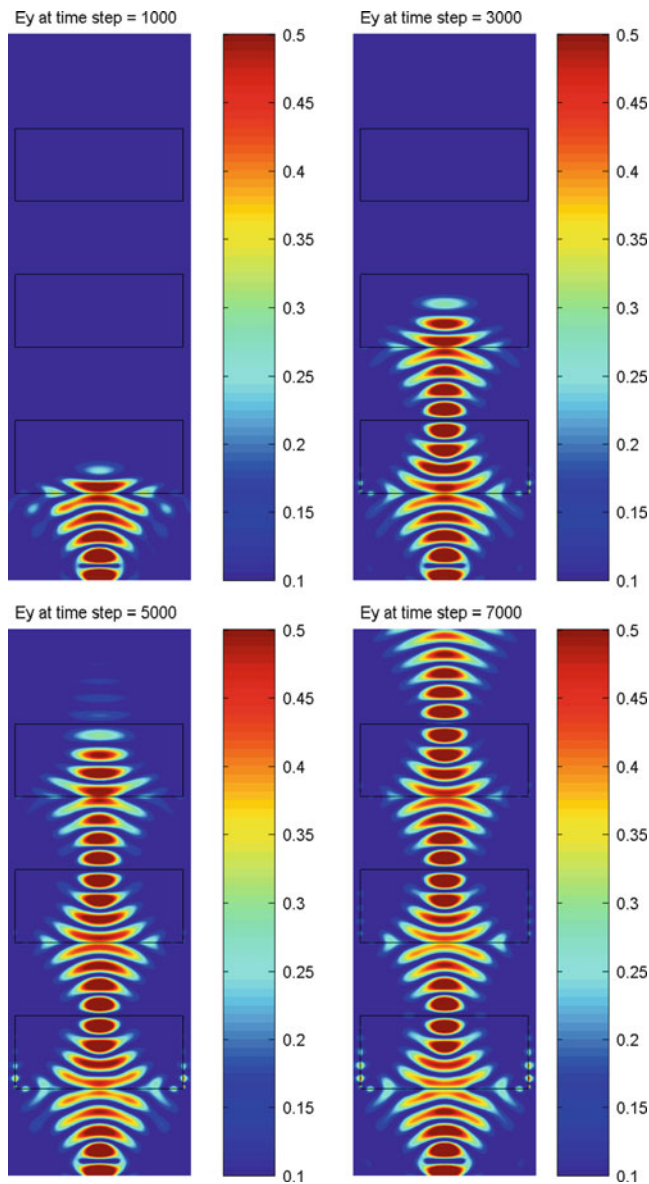
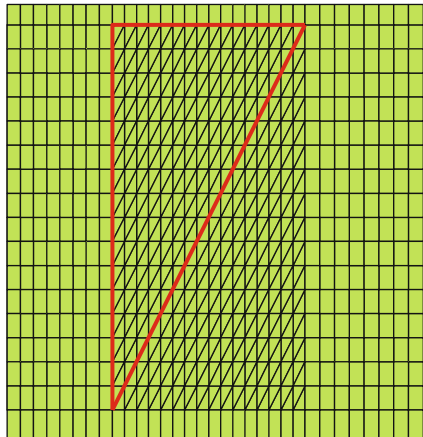


Fig. 9.5 Electric field intensity distribution interacting with three metamaterial slabs of $n \approx -1$ (Reprinted from Li et al. [191]. Copyright (2008), with permission from Elsevier)

order triangular edge element and rectangular edge element are used. Details about the algorithm and implementation can be found in the original paper [157].

An exemplary mesh is shown in Fig. 9.6, which is quite coarse for illustration purpose. The results presented in Fig. 9.7 uses a mesh by uniformly refining Fig. 9.6

Fig. 9.6 An exemplary mixed mesh used for the triangular metamaterial slab



four times, i.e., the real mesh has 131,072 and 81,920 triangular and rectangular elements, respectively. Hence the total number of degrees of freedom for \mathbf{E} is 361,248. In this case, the time step $\tau = 10^{-13}$. The calculated E_y components at various time steps are plotted in Fig. 9.7, which shows clearly that the wave propagates backward inside the metamaterial slab. After the wave exits the metamaterial region, the wave bends according to the Snell's law (1.1).

9.2 Metamaterial Electromagnetic Cloak

In recent years, inspired by the pioneering work of Pendry et al. [237] and Leonhardt [180] in 2006, there is a growing interest in the study of using metamaterials to construct invisibility cloaks of different shapes. More details and references on cloaking can be found in recent reviews [73, 132, 135]. One of the major avenues towards electromagnetic and acoustic cloaking is the so-called transformation optics [180, 237], which uses the coordinate transformation to design the material parameters to steer the light around the cloaked regions. In this section, we present some cloaking results obtained via Maxwell's equations, although cloaking can be achieved through solving other types of equations (e.g., [9, 166, 167])

9.2.1 Form Invariant Property for Maxwell's Equations

Modeling of electromagnetic phenomena at a fixed frequency ω is governed by the full Maxwell's equations (assuming a time harmonic variation of $\exp(j\omega t)$):

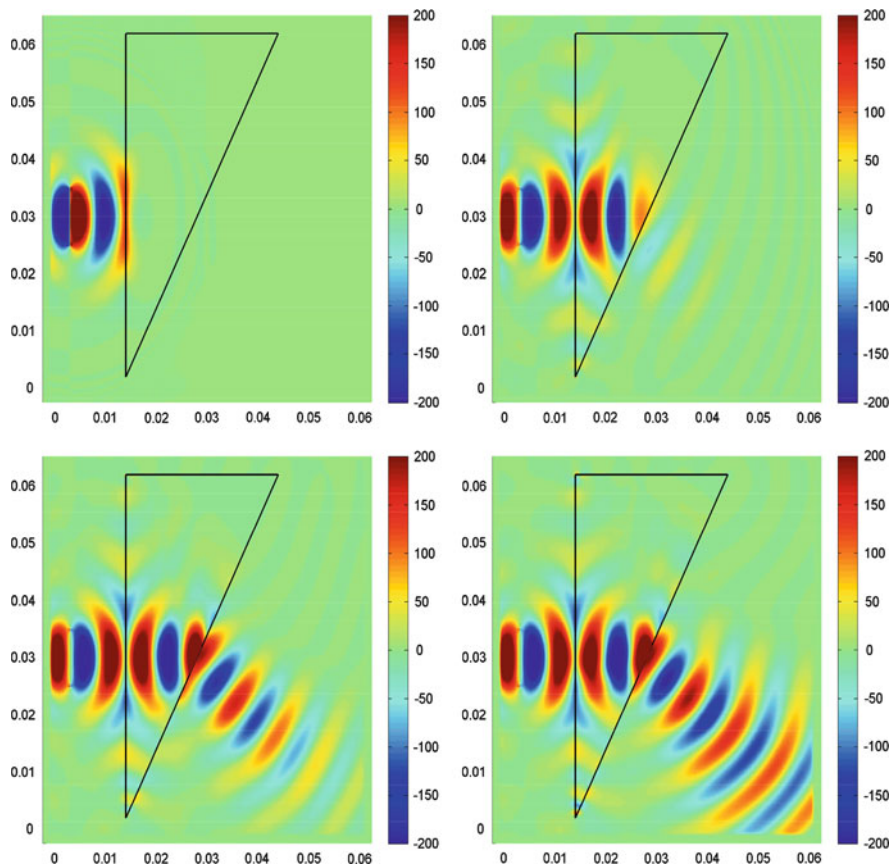


Fig. 9.7 Example 4. Electric fields E_y at various time steps: (Top Left) 800 steps; (Top Right) 2,000 steps; (Bottom Left) 3,000 steps; (Bottom Right) 4,000 steps

$$\nabla \times \mathbf{E} + j\omega\mu\mathbf{H} = 0, \quad \nabla \times \mathbf{H} - j\omega\epsilon\mathbf{E} = 0, \quad (9.22)$$

where $\mathbf{E}(\mathbf{x})$ and $\mathbf{H}(\mathbf{x})$ are the electric and magnetic fields in the frequency domain, and ϵ and μ are the permittivity and permeability of the material.

A very important property for Maxwell's equations is that Maxwell's equations are form invariant under coordinate transformations (cf. [214]). More specifically, we have

Theorem 9.1. *Under a coordinate transformation $\mathbf{x}' = \mathbf{x}'(\mathbf{x})$, the equations (9.22) keep the same form in the transformed coordinate system:*

$$\nabla' \times \mathbf{E}' + j\omega\mu'\mathbf{H}' = 0, \quad \nabla' \times \mathbf{H}' - j\omega\epsilon'\mathbf{E}' = 0, \quad (9.23)$$

where all new variables are given by

$$\mathbf{E}'(\mathbf{x}') = A^{-T} \mathbf{E}(\mathbf{x}), \mathbf{H}'(\mathbf{x}') = A^{-T} \mathbf{H}(\mathbf{x}), A = (a_{ij}), a_{ij} = \frac{\partial x'_i}{\partial x_j}, \quad (9.24)$$

and

$$\mu'(\mathbf{x}') = A\mu(\mathbf{x})A^T / \det(A), \quad \epsilon'(\mathbf{x}') = A\epsilon(\mathbf{x})A^T / \det(A). \quad (9.25)$$

Proof. From (9.24), (9.25) and (9.22), we have

$$j\omega\mu'\mathbf{H}' = j\omega A\mu\mathbf{H} / \det(A) = -A\nabla \times \mathbf{E} / \det(A).$$

Hence to prove the first identity of (9.23), we just need to show that

$$A\nabla \times \mathbf{E} = \det(A) \cdot \nabla' \times \mathbf{E}'. \quad (9.26)$$

Before we prove (9.26), let us recall the 3-D Levi-Civita symbol ϵ_{ijk} , which is 1 if (i, j, k) is an even permutation of $(1, 2, 3)$, -1 if it is an odd permutation, and 0 if any index is repeated. Hence by using the Einstein notation (i.e., omitting the summation symbols), we have

$$\det(A) = \epsilon_{ijk} \frac{\partial x'_1}{\partial x_i} \frac{\partial x'_2}{\partial x_j} \frac{\partial x'_3}{\partial x_k}, \quad (9.27)$$

and the i th component of $\nabla \times \mathbf{E}$:

$$(\nabla \times \mathbf{E})_i = \epsilon_{ijk} \frac{\partial E_k}{\partial x_j},$$

from which and $\mathbf{E} = A^T \mathbf{E}'$, we obtain

$$\begin{aligned} (A\nabla \times \mathbf{E})_i &= \frac{\partial x'_i}{\partial x_m} \epsilon_{mjk} \frac{\partial E_k}{\partial x_j} = \frac{\partial x'_i}{\partial x_m} \epsilon_{mjk} \frac{\partial}{\partial x_j} \left(\frac{\partial x'_l}{\partial x_k} E'_l \right) \\ &= \frac{\partial x'_i}{\partial x_m} \epsilon_{mjk} \left(\frac{\partial^2 x'_l}{\partial x_j \partial x_k} E'_l + \frac{\partial x'_l}{\partial x_k} \frac{\partial E'_l}{\partial x_j} \right) \\ &= \frac{\partial x'_i}{\partial x_m} \epsilon_{mjk} \frac{\partial x'_l}{\partial x_k} \frac{\partial E'_l}{\partial x_j} \\ &= \frac{\partial x'_i}{\partial x_m} \epsilon_{mjk} \frac{\partial x'_l}{\partial x_k} \frac{\partial E'_l}{\partial x'_p} \frac{\partial x'_p}{\partial x_j}, \end{aligned} \quad (9.28)$$

where in the above we used the fact that the first term is zero by swapping the indices j and k .

On the other hand, we have

$$\det(A) \cdot (\nabla' \times \mathbf{E}')_i = \det(A) \cdot \epsilon_{ipl} \frac{\partial E'_l}{\partial x'_p}. \quad (9.29)$$

Comparing (9.28) with (9.29), we can see that proof of (9.26) boils down to proof of the following

$$\frac{\partial x'_i}{\partial x_m} \epsilon_{mjk} \frac{\partial x'_l}{\partial x_k} \frac{\partial x'_p}{\partial x_j} = \det(A) \cdot \epsilon_{ipl},$$

which is true by checking different i, p, l . For example, $i = 1, p = 2, l = 3$ is just (9.27). \square

9.2.2 Design of Cylindrical and Square Cloaks

In this subsection, we present detailed derivation of the metamaterial's permittivity and permeability which lead to cloaking phenomena. The contents of this subsection are mainly based on [188].

9.2.2.1 Cylindrical Cloak

Following [237], to hide an object inside the cylindrical region $r \leq R_1$, a special electromagnetic metamaterial can be designed in the cloaking region $R_1 < r < R_2$ through the so-called transformation optics technique. The idea is to take all fields in the region $r < R_2$ and compress them into the region $R_1 < r < R_2$. This can be accomplished by the following simple coordinate transformation:

$$r'(r, \theta) = \frac{R_2 - R_1}{R_2} r + R_1, \quad 0 \leq r \leq R_2, \quad (9.30)$$

$$\theta'(r, \theta) = \theta. \quad (9.31)$$

To carry out a cloaking simulation in Cartesian coordinates, we have to transform the material parameters given in polar coordinates to Cartesian coordinates. It is known that a point (x_1, x_2) in the Cartesian coordinate system corresponds to a point (r, θ) in polar coordinate system through the relations:

$$r = \sqrt{x_1^2 + x_2^2}, \quad \theta = \tan^{-1} \frac{x_2}{x_1}, \quad (9.32)$$

and

$$x_1 = r \cos \theta, \quad x_2 = r \sin \theta, \quad (9.33)$$

which leads to

$$\frac{\partial r}{\partial x_1} = \frac{x_1}{r} = \cos \theta, \quad \frac{\partial r}{\partial x_2} = \frac{x_2}{r} = \sin \theta, \quad (9.34)$$

$$\frac{\partial \theta}{\partial x_1} = -\frac{x_2}{r^2} = -\frac{\sin \theta}{r}, \quad \frac{\partial \theta}{\partial x_2} = \frac{x_1}{r^2} = \frac{\cos \theta}{r}. \quad (9.35)$$

By Theorem 9.1, the electromagnetic permittivity and permeability in the transformed space are given by (9.25), which needs the information of $\frac{\partial x'_i}{\partial x_j}$. For the transformation (9.30) and (9.31), by chain rule we can obtain

$$\begin{aligned} (i) \quad \frac{\partial x'_1}{\partial x_1} &= \frac{\partial x'_1}{\partial r'} \frac{\partial r'}{\partial r} \frac{\partial r}{\partial x_1} + \frac{\partial x'_1}{\partial \theta'} \frac{\partial \theta'}{\partial \theta} \frac{\partial \theta}{\partial x_1} \\ &= \cos \theta \cdot \frac{R_2 - R_1}{R_2} \cdot \cos \theta - r' \sin \theta \cdot \left(-\frac{\sin \theta}{r}\right) \\ &= \frac{R_2 - R_1}{R_2} + \frac{R_1}{r} \sin^2 \theta, \end{aligned}$$

$$\begin{aligned} (ii) \quad \frac{\partial x'_1}{\partial x_2} &= \frac{\partial x'_1}{\partial r'} \frac{\partial r'}{\partial r} \frac{\partial r}{\partial x_2} + \frac{\partial x'_1}{\partial \theta'} \frac{\partial \theta'}{\partial \theta} \frac{\partial \theta}{\partial x_2} \\ &= \cos \theta \cdot \frac{R_2 - R_1}{R_2} \cdot \sin \theta - r' \sin \theta \cdot \left(\frac{\cos \theta}{r}\right) \\ &= -\frac{R_1}{r} \sin \theta \cos \theta, \end{aligned}$$

$$\begin{aligned} (iii) \quad \frac{\partial x'_2}{\partial x_1} &= \frac{\partial x'_2}{\partial r'} \frac{\partial r'}{\partial r} \frac{\partial r}{\partial x_1} + \frac{\partial x'_2}{\partial \theta'} \frac{\partial \theta'}{\partial \theta} \frac{\partial \theta}{\partial x_1} \\ &= \sin \theta \cdot \frac{R_2 - R_1}{R_2} \cdot \cos \theta + r' \cos \theta \cdot \left(-\frac{\sin \theta}{r}\right) \\ &= -\frac{R_1}{r} \sin \theta \cos \theta, \end{aligned}$$

and

$$\begin{aligned} (iv) \quad \frac{\partial x'_2}{\partial x_2} &= \frac{\partial x'_2}{\partial r'} \frac{\partial r'}{\partial r} \frac{\partial r}{\partial x_2} + \frac{\partial x'_2}{\partial \theta'} \frac{\partial \theta'}{\partial \theta} \frac{\partial \theta}{\partial x_2} \\ &= \sin \theta \cdot \frac{R_2 - R_1}{R_2} \cdot \sin \theta + r' \cos \theta \cdot \left(\frac{\cos \theta}{r}\right) \\ &= \frac{R_2 - R_1}{R_2} + \frac{R_1}{r} \cos^2 \theta. \end{aligned}$$

Hence by Theorem 9.1, the transformation matrix A can be obtained as

$$A = \begin{pmatrix} \frac{R_2-R_1}{R_2} + \frac{R_1}{r} \sin^2 \theta & -\frac{R_1}{r} \sin \theta \cos \theta \\ \text{symmetric} & \frac{R_2-R_1}{R_2} + \frac{R_1}{r} \cos^2 \theta \end{pmatrix}, \quad (9.36)$$

whose determinant is

$$\det(A) = \frac{R_2 - R_1}{R_2} \left(\frac{R_2 - R_1}{R_2} + \frac{R_1}{r} \right) = \left(\frac{R_2 - R_1}{R_2} \right)^2 \cdot \frac{r'}{r' - R_1}. \quad (9.37)$$

Substituting (9.36) and (9.37) into (9.25) with relative permittivity $\epsilon_r = 1$ in the original space, we obtain the relative permittivity in the transformed space

$$\begin{aligned} \epsilon' &= \begin{pmatrix} \epsilon'_{xx} & \epsilon'_{xy} \\ \epsilon'_{yx} & \epsilon'_{yy} \end{pmatrix} = AA^T / \det(A) \\ &= \begin{pmatrix} \left(\frac{R_2-R_1}{R_2} \right)^2 + \frac{R_1}{r} \left(2 \frac{R_2-R_1}{R_2} + \frac{R_1}{r} \right) \sin^2 \theta & -\frac{R_1}{r} \left(2 \frac{R_2-R_1}{R_2} + \frac{R_1}{r} \right) \sin \theta \cos \theta \\ \text{symmetric} & \left(\frac{R_2-R_1}{R_2} \right)^2 + \frac{R_1}{r} \left(2 \frac{R_2-R_1}{R_2} + \frac{R_1}{r} \right) \cos^2 \theta \end{pmatrix} / \det(A), \end{aligned}$$

i.e., the material parameters in Cartesian coordinates become as follows:

$$\begin{aligned} \epsilon'_{xx} &= \left[\left(\frac{R_2 - R_1}{R_2} \right)^2 + \frac{R_1}{r} \left(2 \frac{R_2 - R_1}{R_2} + \frac{R_1}{r} \right) \sin^2 \theta \right] / \det(A), \\ \epsilon'_{xy} &= \epsilon'_{yx} = \left[-\frac{R_1}{r} \left(2 \frac{R_2 - R_1}{R_2} + \frac{R_1}{r} \right) \sin \theta \cos \theta \right] / \det(A), \\ \epsilon'_{yy} &= \left[\left(\frac{R_2 - R_1}{R_2} \right)^2 + \frac{R_1}{r} \left(2 \frac{R_2 - R_1}{R_2} + \frac{R_1}{r} \right) \cos^2 \theta \right] / \det(A), \end{aligned}$$

and $\epsilon'_z = 1/\det(A)$. The permeability μ' has the same form as permittivity ϵ' .

9.2.2.2 Square Cloak

The transformation optics idea can be used for designing a square-shaped cloak. In this case, the fields inside a square with width $2S_2$ are compressed into a square annulus with inner square width $2S_1$ and outer square width $2S_2$. This task can be accomplished through four mappings.

The right triangle in the original space is mapped into the right-subdomain in the transformed space (see Fig. 9.8) by the coordinate transformation [244]

$$x'_1(x_1, x_2) = x_1 \frac{S_2 - S_1}{S_2} + S_1, \quad (9.38)$$

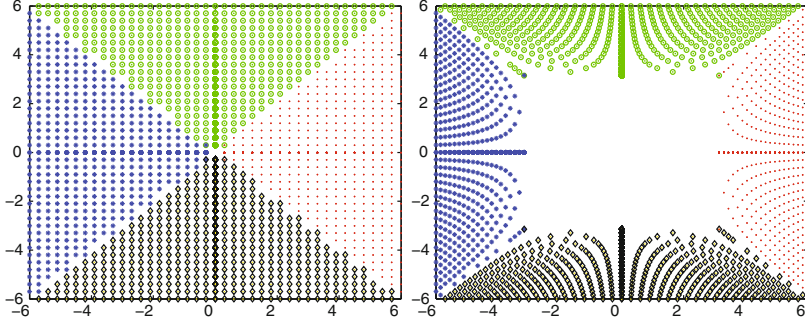


Fig. 9.8 (Left) The original *square* formed by four *triangles*; (Right) The transformed *square annulus*

$$x'_2(x_1, x_2) = x_2 \left(\frac{S_2 - S_1}{S_2} + \frac{S_1}{x_1} \right). \quad (9.39)$$

It is easy to prove that the transformation matrix in this case is

$$A_r = \begin{pmatrix} \frac{S_2 - S_1}{S_2} & 0 \\ -\frac{x_2 S_1}{x_1^2} & \frac{S_2 - S_1}{S_2} + \frac{S_1}{x_1} \end{pmatrix}, \quad (9.40)$$

which has determinant

$$\det(A_r) = \frac{S_2 - S_1}{S_2} \left(\frac{S_2 - S_1}{S_2} + \frac{S_1}{x_1} \right). \quad (9.41)$$

Mapping the unit permittivity tensor $\epsilon = I$ by (9.25), we obtain

$$\epsilon'_r = A_r A_r^T / \det(A_r) = \begin{pmatrix} \left(\frac{S_2 - S_1}{S_2} \right)^2 & -\frac{x_2 S_1}{x_1^2} \cdot \frac{S_2 - S_1}{S_2} \\ \text{symmetric} & \left(\frac{x_2 S_1}{x_1^2} \right)^2 + \left(\frac{S_2 - S_1}{S_2} + \frac{S_1}{x_1} \right)^2 \end{pmatrix} / \det(A_r). \quad (9.42)$$

Corresponding formulas for the upper, left and bottom sub-domains of the cloak can be similarly obtained by applying rotation matrix $R(\theta) = \begin{bmatrix} \cos \theta & -\sin \theta \\ \sin \theta & \cos \theta \end{bmatrix}$ to the right sub-domain with rotation angles $\theta = \pi/2, \pi$ and $3\pi/2$, respectively.

More specifically, for the upper subdomain, we have

$$\epsilon'_u = R\left(\frac{\pi}{2}\right) \epsilon'_r R\left(\frac{\pi}{2}\right)^T = \begin{pmatrix} \left(\frac{S_2 - S_1}{S_2} + \frac{S_1}{x_1} \right)^2 + \left(\frac{x_2 S_1}{x_1^2} \right)^2 & \frac{S_2 - S_1}{S_2} \cdot \frac{x_2 S_1}{x_1^2} \\ \text{symmetric} & \left(\frac{S_2 - S_1}{S_2} \right)^2 \end{pmatrix} / \det(A_r).$$

For the left subdomain, we have

$$\epsilon'_l = R(\pi)\epsilon'_r R(\pi)^T = \begin{pmatrix} (\frac{S_2-S_1}{S_2})^2 & -\frac{x_2 S_1}{x_1^2} \cdot \frac{S_2-S_1}{S_2} \\ \text{symmetric} & (\frac{x_2 S_1}{x_1^2})^2 + (\frac{S_2-S_1}{S_2} + \frac{S_1}{x_1})^2 \end{pmatrix} / \det(A_r).$$

For the bottom subdomain, we have

$$\epsilon'_b = R(\frac{3\pi}{2})\epsilon'_r R(\frac{3\pi}{2})^T = \begin{pmatrix} (\frac{S_2-S_1}{S_2} + \frac{S_1}{x_1})^2 + (\frac{x_2 S_1}{x_1^2})^2 & \frac{S_2-S_1}{S_2} \cdot \frac{x_2 S_1}{x_1^2} \\ \text{symmetric} & (\frac{S_2-S_1}{S_2})^2 \end{pmatrix} / \det(A_r).$$

9.2.3 Cloak Simulation in the Frequency Domain

Before we move to the time domain cloak simulation in the next section, here we present some 2-D cloaking simulations in the frequency domain. Without loss of generality, we consider the 2-D transverse magnetic model. Reducing (9.22) with $\epsilon = \epsilon_0 \epsilon_r$ and $\mu = \mu_0 \mu_r$ into just one equation involving the scalar variable E_z , we obtain

$$\nabla \times (\mu_r^{-1} \nabla \times E_z) - k_0^2 \epsilon_r E_z = 0, \quad (9.43)$$

where μ_r and ϵ_r are the relative permeability and permittivity, and k_0 denotes the wave number of free space $k_0 = \omega \sqrt{\epsilon_0 \mu_0} = \frac{\omega}{C_v}$. As before, $C_v = 1/\sqrt{\epsilon_0 \mu_0}$ denotes the light speed in free space.

The simulations given below are performed by COMSOL Multiphysics package, where quadratic triangular elements and the direct solver SPOOLES are used.

9.2.3.1 Cylindrical Cloak

For this test, the cylinder cloak shell is chosen to have $R_1 = 0.15$ m and $R_2 = 0.3$ m, and located inside the square $[-1.0, 1.0]^2$. A PML with 0.5 m thickness is imposed on both ends of this square in the x -direction, and the periodic boundary is imposed on the top and bottom boundaries. The incident plane waves of 1–4 GHz are excited on the interface $x = -1$.

First, a coarse mesh with 14,624 elements and 7,417 nodes is used for the simulation. In this case, the total number of DOFs is 25,584. The obtained electric field distributions for incident waves of several frequencies are presented in Fig. 9.9, which show that the 1–3 GHz plane wave patterns are restored quite well after the waves propagate out of the cloaked area. Hence this structure demonstrates good cloaking effect for 1–3 GHz plane waves. However, the cloaking phenomenon is not clear for the 4 GHz incident wave.

Then the same problem is solved again with a finer mesh obtained by uniformly refining the previous mesh twice, in which case the mesh has 58,496 elements, 29,457 nodes and 101,728 DOFs. With this finer mesh, the cloaking effect can be seen quite clearly for all 1–4 GHz incident waves as demonstrated in Fig. 9.10.

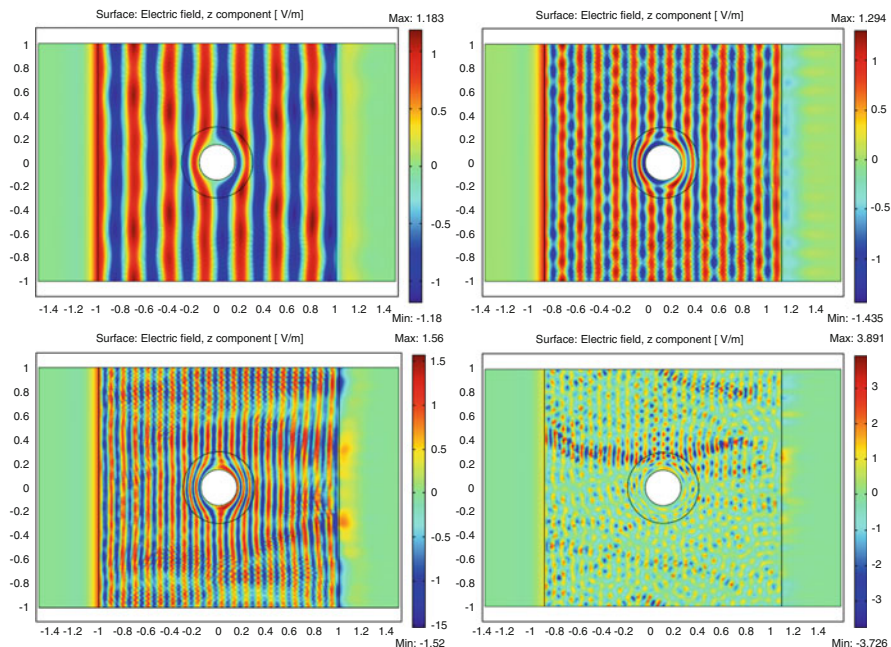


Fig. 9.9 The real part of the electric-field phasor obtained for the cylinder cloak with incident waves of different frequencies: (*Top Left*) 1 GHz; (*Top Right*) 2 GHz; (*Bottom Left*) 3 GHz; (*Bottom Right*) 4 GHz

9.2.3.2 Square Cloak

The square cloak has the same geometry as the cylindrical case, except that the circular shell is replaced by a rectangular shell. This problem is solved first using a mesh with 7,200 elements, 3,720 nodes and 11,352 DOFs, and the cloaking effect can be seen only for waves with 1 and 2 GHz frequencies. Then the problem is solved again using a finer mesh refined uniformly from the previous one, and the cloaking effect can be seen for waves with 3 and 4 GHz frequencies. In Fig. 9.11, the obtained electric field distributions for 3 and 4 GHz waves are presented for both the coarse and fine meshes. This example shows that modeling wave propagation in metamaterials is quite challenging, since the right physical phenomena can be observed only when the mesh is fine enough.

9.3 Time Domain Cloak Simulation

Compared to many frequency domain cloak simulations, not much attention has been paid to the time-domain modeling of cloaks. Since 2008, some papers have

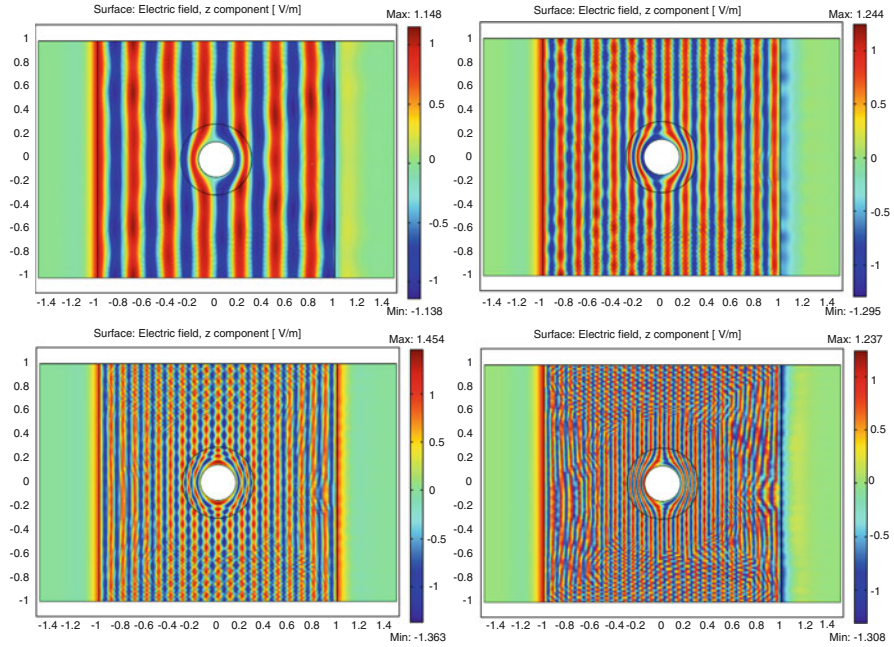


Fig. 9.10 The real part of the electric-field phasor obtained for the cylinder cloak with a fine mesh and various incident waves: (*Top Left*) 1 GHz; (*Top Right*) 2 GHz; (*Bottom Left*) 3 GHz; (*Bottom Right*) 4 GHz

been published on time-domain simulation of 2-D cloaking structures (see [197, 303, 304] and references therein). The recently designed broadband cloaks by Liu et al. in 2009 [206] make the time-domain simulation more appealing and necessary. Inspired by the work of [304], Li et al. [194] developed the first time-domain finite element (FETD) scheme for cloak simulation. This section is mainly based on [194].

9.3.1 The Governing Equations

Following [304], the time-domain cloak modeling is based on equations:

$$\frac{\partial \mathbf{B}}{\partial t} = -\nabla \times \mathbf{E}, \quad (9.44)$$

$$\frac{\partial \mathbf{D}}{\partial t} = \nabla \times \mathbf{H}, \quad (9.45)$$

and the constitutive relations

$$\mathbf{D} = \epsilon \mathbf{E}, \quad (9.46)$$

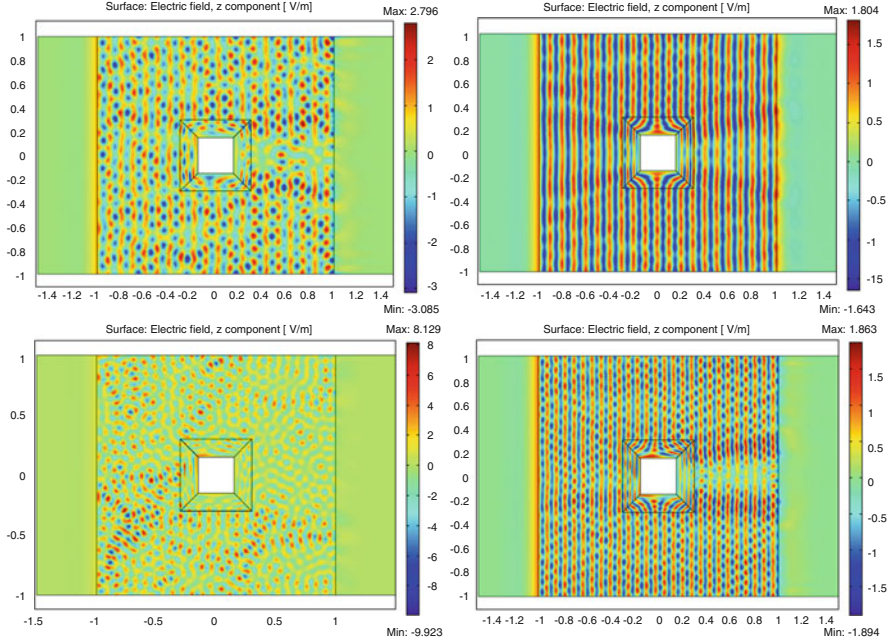


Fig. 9.11 The real part of the electric-field phasor obtained for the *square* cloak under two meshes: (Top Row) 3 GHz wave; (Bottom Row) 4 GHz wave

$$\mathbf{B} = \mu \mathbf{H}, \quad (9.47)$$

where as usual \mathbf{E} and \mathbf{H} are the electric and magnetic fields respectively, \mathbf{D} and \mathbf{B} are the electric displacement and magnetic induction respectively, ϵ and μ are cloak permittivity and permeability, respectively. For the cylindrical cloak, the ideal material parameters in the polar coordinate system were first given by Pendry et al. [237]:

$$\epsilon_r = \mu_r = \frac{r - R_1}{r}, \quad \epsilon_\phi = \mu_\phi = \frac{r}{r - R_1}, \quad \epsilon_z = \mu_z = \left(\frac{R_2}{R_2 - R_1} \right)^2 \frac{r - R_1}{r}, \quad (9.48)$$

where R_1 and R_2 are the inner and outer radius of the cloak. From (9.48), it can be seen that the cloaking metamaterial's permittivity and permeability are nonhomogeneous and highly anisotropic.

Following [304], here we consider the 2-D case with \mathbf{E} being a vector, and \mathbf{H} being a scalar, i.e., we can write $\mathbf{E} = (E_x, E_y)'$ and $H = H_z$, where the subindex x, y or z denotes the component in each direction. To carry out the simulation in Cartesian coordinates, we have to transform the material parameters (9.48) into Cartesian coordinates. It is easy to see that

$$\begin{aligned} \begin{bmatrix} \epsilon_{xx} & \epsilon_{xy} \\ \epsilon_{yx} & \epsilon_{yy} \end{bmatrix} &= \begin{bmatrix} \cos \phi & -\sin \phi \\ \sin \phi & \cos \phi \end{bmatrix} \cdot \begin{bmatrix} \epsilon_r & 0 \\ 0 & \epsilon_\phi \end{bmatrix} \cdot \begin{bmatrix} \cos \phi & \sin \phi \\ -\sin \phi & \cos \phi \end{bmatrix} \\ &= \begin{bmatrix} \epsilon_r \cos^2 \phi + \epsilon_\phi \sin^2 \phi & (\epsilon_r - \epsilon_\phi) \sin \phi \cos \phi \\ (\epsilon_r - \epsilon_\phi) \sin \phi \cos \phi & \epsilon_r \sin^2 \phi + \epsilon_\phi \cos^2 \phi \end{bmatrix}, \end{aligned}$$

which, along with $\epsilon_0 \begin{bmatrix} E_x \\ E_y \end{bmatrix} = \begin{bmatrix} \epsilon_{xx} & \epsilon_{xy} \\ \epsilon_{yx} & \epsilon_{yy} \end{bmatrix}^{-1} \begin{bmatrix} D_x \\ D_y \end{bmatrix}$, yields

$$\epsilon_0 \epsilon_r \epsilon_\phi \mathbf{E} = \begin{bmatrix} \epsilon_r \sin^2 \phi + \epsilon_\phi \cos^2 \phi & (\epsilon_\phi - \epsilon_r) \sin \phi \cos \phi \\ (\epsilon_\phi - \epsilon_r) \sin \phi \cos \phi & \epsilon_r \cos^2 \phi + \epsilon_\phi \sin^2 \phi \end{bmatrix} \mathbf{D}. \quad (9.49)$$

To obtain the cloak phenomenon, the material parameters have to be constructed from dispersive medium models. For simplicity, we consider the Drude model for the permittivity:

$$\epsilon_r(\omega) = 1 - \frac{\omega_p^2}{\omega^2 - j\omega\gamma}, \quad (9.50)$$

where $\gamma \geq 0$ and $\omega_p > 0$ are the collision and plasma frequencies, respectively. Substituting (9.50) into (9.49) and using the following rules

$$j\omega \rightarrow \frac{\partial}{\partial t}, \quad \omega^2 \rightarrow -\frac{\partial^2}{\partial t^2}, \quad (9.51)$$

we have (cf. [304]):

$$\begin{aligned} &\epsilon_0 \epsilon_\phi \left(\frac{\partial^2}{\partial t^2} + \gamma \frac{\partial}{\partial t} + \omega_p^2 \right) \mathbf{E} \\ &= \left(\frac{\partial^2}{\partial t^2} + \gamma \frac{\partial}{\partial t} + \omega_p^2 \right) M_A \mathbf{D} + \epsilon_\phi \left(\frac{\partial^2}{\partial t^2} + \gamma \frac{\partial}{\partial t} \right) M_B \mathbf{D}, \end{aligned} \quad (9.52)$$

where the vector $\mathbf{D} = (D_x, D_y)'$ and

$$M_A = \begin{bmatrix} \sin^2 \phi & -\sin \phi \cos \phi \\ -\sin \phi \cos \phi & \cos^2 \phi \end{bmatrix}, \quad M_B = \begin{bmatrix} \cos^2 \phi & \sin \phi \cos \phi \\ \sin \phi \cos \phi & \sin^2 \phi \end{bmatrix}.$$

Similarly, the permeability is described by the Drude model [304]:

$$\mu_z(\omega) = A \left(1 - \frac{\omega_{pm}^2}{\omega^2 - j\omega\gamma_m} \right), \quad (9.53)$$

where $A = \frac{R_2}{R_2 - R_1}$, and $\omega_{pm} > 0$ and $\gamma_m \geq 0$ are the magnetic plasma and collision frequencies, respectively. Substituting (9.53) into (9.47), we obtain

$$B_z = \mu_o \mu_z H_z = \mu_o A \left(1 - \frac{\omega_{pm}^2}{\omega^2 - j\omega\gamma_m} \right) H_z.$$

Then using rules (9.51), we have

$$\left(\frac{\partial^2}{\partial t^2} + \gamma_m \frac{\partial}{\partial t} \right) B_z = \mu_o A \left(\frac{\partial^2}{\partial t^2} + \gamma_m \frac{\partial}{\partial t} + \omega_{pm}^2 \right) H_z. \quad (9.54)$$

To carry out the cloak simulation, we use Bérenger's PML [34] to reduce the infinite domain to a bounded one by absorbing those waves leaving the computational domain without introducing reflections. The two dimensional Bérenger PML governing equations can be written as:

$$\varepsilon_0 \frac{\partial E_x}{\partial t} + \sigma_y E_x = \frac{\partial (H_{zx} + H_{zy})}{\partial y}, \quad (9.55)$$

$$\varepsilon_0 \frac{\partial E_y}{\partial t} + \sigma_x E_y = -\frac{\partial (H_{zx} + H_{zy})}{\partial x}, \quad (9.56)$$

$$\mu_0 \frac{\partial H_{zx}}{\partial t} + \sigma_{mx} H_{zx} = -\frac{\partial E_y}{\partial x}, \quad (9.57)$$

$$\mu_0 \frac{\partial H_{zy}}{\partial t} + \sigma_{my} H_{zy} = \frac{\partial E_x}{\partial y}, \quad (9.58)$$

where the parameters $\sigma_i, \sigma_{mi}, i = x, y$, are the homogeneous electric and magnetic conductivities in the x and y directions, respectively.

For implementation purpose, (9.55) and (9.56) is written in the vector form:

$$\varepsilon_0 \frac{\partial \mathbf{E}}{\partial t} + \begin{pmatrix} \sigma_y & 0 \\ 0 & \sigma_x \end{pmatrix} \mathbf{E} = \nabla \times \mathbf{H}, \quad (9.59)$$

where the 2-D vector curl operator $\nabla \times \mathbf{H} = \begin{pmatrix} \frac{\partial H}{\partial y} \\ -\frac{\partial H}{\partial x} \end{pmatrix}$ for $\mathbf{H} = H_{zx} + H_{zy}$.

9.3.2 An Explicit Finite Element Scheme

To design the scheme, we partition Ω by a family of regular meshes T_h with maximum mesh size h . To accommodate the problem easily, a hybrid mesh is used: triangles in both cloaking and free space regions; rectangles in the PML region, cf. Fig. 9.12b below. The basis functions used are the lowest-order Raviart-Thomas-Nédélec's mixed spaces \mathbf{U}_h and \mathbf{V}_h : For a rectangular mesh T_h , we choose

$$\begin{aligned}\mathbf{U}_h &= \{\psi_h \in L^2(\Omega) : \psi_h|_K \in Q_{0,0}, \forall K \in T_h\}, \\ \mathbf{V}_h &= \{\phi_h \in H(\text{curl}; \Omega) : \phi_h|_K \in Q_{0,1} \times Q_{1,0}, \forall K \in T_h\};\end{aligned}$$

while on a triangular mesh,

$$\begin{aligned}\mathbf{U}_h &= \{\psi_h \in L^2(\Omega) : \psi_h|_K \text{ is a piecewise constant}, \forall K \in T_h\}, \\ \mathbf{V}_h &= \{\phi_h \in H(\text{curl}; \Omega) : \phi_h|_K = \text{span}\{\lambda_i \nabla \lambda_j - \lambda_j \nabla \lambda_i\}, i, j = 1, 2, 3, \forall K \in T_h\}.\end{aligned}$$

To accommodate the perfect conducting boundary condition $\mathbf{n} \times \mathbf{E} = \mathbf{0}$, we introduce the subspace of \mathbf{V}_h :

$$\mathbf{V}_h^0 = \{\phi_h \in \mathbf{V}_h, \mathbf{n} \times \phi_h = \mathbf{0} \text{ on } \partial\Omega\}.$$

Following [194], a leap-frog type scheme can be constructed for the modeling equations in the cloak region: For $n = 1, 2, \dots$, find $\mathbf{D}_h^{n+\frac{1}{2}}, \mathbf{E}_h^{n+\frac{1}{2}} \in \mathbf{V}_h^0$, $\mathbf{B}_h^{n+1}, \mathbf{H}_h^{n+1} \in \mathbf{U}_h$ such that

$$\left(\delta_\tau \mathbf{D}_h^{n+\frac{1}{2}}, \phi_h \right) - (H_h^n, \nabla \times \phi_h) = 0, \quad (9.60)$$

$$\begin{aligned}& \left(\varepsilon_0 \varepsilon_\phi \delta_\tau^2 \mathbf{E}_h^{n+\frac{1}{2}}, \widetilde{\phi}_h \right) + \left(\gamma \varepsilon_0 \varepsilon_\phi \delta_{2\tau} \mathbf{E}_h^{n+\frac{1}{2}}, \widetilde{\phi}_h \right) + \left(\omega_p^2 \varepsilon_0 \varepsilon_\phi \overline{\mathbf{E}}_h^{n-\frac{1}{2}}, \widetilde{\phi}_h \right) \\ &= \left((M_A + \varepsilon_\phi M_B) \delta_\tau^2 \mathbf{D}_h^{n+\frac{1}{2}}, \widetilde{\phi}_h \right) + \left(\omega_p^2 M_A \overline{\mathbf{D}}_h^{n-\frac{1}{2}}, \widetilde{\phi}_h \right) \\ & \quad + \left(\gamma (M_A + \varepsilon_\phi M_B) \delta_{2\tau} \mathbf{D}_h^{n+\frac{1}{2}}, \widetilde{\phi}_h \right),\end{aligned} \quad (9.61)$$

$$(\delta_\tau \mathbf{B}_h^{n+1}, \psi_h) + \left(\nabla \times \mathbf{E}_h^{n+\frac{1}{2}}, \psi_h \right) = 0, \quad (9.62)$$

$$\begin{aligned}& (\mu_0 A \delta_\tau^2 H_h^{n+1}, \widetilde{\psi}_h) + (\mu_0 A \gamma_m \delta_{2\tau} H_h^{n+1}, \widetilde{\psi}_h) + (\mu_0 A \omega_{pm}^2 \overline{H}_h^n, \widetilde{\psi}_h) \\ &= (\delta_\tau^2 \mathbf{B}_h^{n+1}, \widetilde{\psi}_h) + (\gamma_m \delta_{2\tau} \mathbf{B}_h^{n+1}, \widetilde{\psi}_h),\end{aligned} \quad (9.63)$$

hold true for any $\phi_h, \widetilde{\phi}_h \in \mathbf{V}_h^0$, $\psi_h, \widetilde{\psi}_h \in \mathbf{U}_h$. Here and below we denote the difference operators: For any $\mathbf{u}^n = \mathbf{u}(\cdot, t_n)$,

$$\begin{aligned}\delta_\tau \mathbf{u}^n &= \frac{\mathbf{u}^n - \mathbf{u}^{n-1}}{\tau}, \quad \delta_\tau^2 \mathbf{u}^n = \frac{\mathbf{u}^n - 2\mathbf{u}^{n-1} + \mathbf{u}^{n-2}}{\tau^2}, \\ \delta_{2\tau} \mathbf{u}^n &= \frac{\mathbf{u}^n - \mathbf{u}^{n-2}}{2\tau}, \quad \overline{\mathbf{u}}^{n-1} = \frac{\mathbf{u}^n + 2\mathbf{u}^{n-1} + \mathbf{u}^{n-2}}{4}, \quad \widehat{\mathbf{u}}^n = \frac{\mathbf{u}^n + \mathbf{u}^{n-1}}{2}.\end{aligned}$$

To couple (9.63) well with the PML equations (9.57), (9.58), and (9.63) is split into

$$\begin{aligned} & \left(\mu_0 A \delta_\tau^2 H_{zx,h}^{n+1}, \widetilde{\psi}_h \right) + \left(\mu_0 A \gamma_m \delta_{2\tau} H_{zx,h}^{n+1}, \widetilde{\psi}_h \right) + \left(\mu_0 A \omega_{pm}^2 \overline{H}_{zx,h}^n, \widetilde{\psi}_h \right) \\ &= \frac{1}{2} \left(\delta_\tau^2 B_h^{n+1}, \widetilde{\psi}_h \right) + \frac{1}{2} \left(\gamma_m \delta_{2\tau} B_h^{n+1}, \widetilde{\psi}_h \right), \end{aligned} \quad (9.64)$$

$$\begin{aligned} & \left(\mu_0 A \delta_\tau^2 H_{zy,h}^{n+1}, \widetilde{\psi}_h \right) + \left(\mu_0 A \gamma_m \delta_{2\tau} H_{zy,h}^{n+1}, \widetilde{\psi}_h \right) + \left(\mu_0 A \omega_{pm}^2 \overline{H}_{zy,h}^n, \widetilde{\psi}_h \right) \\ &= \frac{1}{2} \left(\delta_\tau^2 B_h^{n+1}, \widetilde{\psi}_h \right) + \frac{1}{2} \left(\gamma_m \delta_{2\tau} B_h^{n+1}, \widetilde{\psi}_h \right). \end{aligned} \quad (9.65)$$

Similarly, a leap-frog type scheme can be constructed for solving the Eqs. (9.59), (9.57), and (9.58) in the PML region: find $\mathbf{E}_h^{n+\frac{1}{2}} \in \mathbf{V}_h^0$, $H_{zx,h}^{n+1}$, $H_{zy,h}^{n+1} \in U_h$ such that

$$\varepsilon_0 \left(\delta_\tau \mathbf{E}_h^{n+\frac{1}{2}}, \widetilde{\phi}_h \right) + \left(\begin{pmatrix} \sigma_y & 0 \\ 0 & \sigma_x \end{pmatrix} \widehat{\mathbf{E}}_h^{n+\frac{1}{2}}, \widetilde{\phi}_h \right) = \left(H_{zx,h}^n + H_{zy,h}^n, \nabla \times \widetilde{\phi}_h \right), \quad (9.66)$$

$$\mu_0 \left(\delta_\tau H_{zx,h}^{n+1}, \psi_{1,h} \right) + \left(\sigma_{mx} \widehat{H}_{zx,h}^{n+1}, \psi_{1,h} \right) = - \left(\frac{\partial}{\partial x} E_{y,h}^{n+\frac{1}{2}}, \psi_{1,h} \right), \quad (9.67)$$

$$\mu_0 \left(\delta_\tau H_{zy,h}^{n+1}, \psi_{2,h} \right) + \left(\sigma_{my} \widehat{H}_{zy,h}^{n+1}, \psi_{2,h} \right) = \left(\frac{\partial}{\partial y} E_{x,h}^{n+\frac{1}{2}}, \psi_{2,h} \right), \quad (9.68)$$

hold true for any $\widetilde{\phi}_h \in \mathbf{V}_h^0$, $\psi_{1,h}, \psi_{2,h} \in U_h$.

In summary, the above developed mixed finite element time-domain algorithm for modeling the invisible cloak can be implemented as follows: first, construct a proper mesh \mathcal{T}_h of Ω , choose a proper time step size τ and proper initial conditions; then at each time step n , perform the **FETD Algorithm**:

1. Solve (9.60) for $\mathbf{D}_h^{n+\frac{1}{2}}$ on \mathcal{T}_h .
2. Solve (9.61) and (9.66) for $\mathbf{E}_h^{n+\frac{1}{2}}$ on \mathcal{T}_h .
3. Solve (9.62) for \mathbf{B}_h^{n+1} on \mathcal{T}_h .
4. Solve (9.64) and (9.67) for $H_{zx,h}^{n+1}$ on \mathcal{T}_h .
5. Solve (9.65) and (9.68) for $H_{zy,h}^{n+1}$ on \mathcal{T}_h .
6. Calculate $H_h^{n+1} = H_{zx,h}^{n+1} + H_{zy,h}^{n+1}$, then go back to step 1 and repeat the above process. Note that in the free space region, $\mathbf{E}_h^{n+\frac{1}{2}}$ and H^{n+1} are updated using (9.66)–(9.68) with $\sigma_x = \sigma_y = \sigma_{mx} = \sigma_{my} = 0$.

9.3.2.1 Time-Domain Cloaking Simulation Results

The cloak simulation setup is shown in Fig. 9.12a, where the cloaked object is hidden inside a perfectly electrically conducting cylinder with radius R_1 , and the cylinder is wrapped by a cylindrical cloak with thickness $R_2 - R_1$.

In the cloak simulation, $R_1 = 0.1$ m, $R_2 = 0.2$ m and $\gamma = \gamma_m = 0$ (i.e., no loss) are used in the Drude model. A plane wave source is specified by the function $H_z = 0.1 \sin(\omega t)$, where $\omega = 2\pi f$ with operating frequency $f = 2$ GHz. The parameters $\omega_p = \omega_{pm}$ is calculated by the Drude model $\omega_p = \omega \sqrt{1 - \epsilon_r}$.

As mentioned in Sect. 9.2.3, in order to see the cloaking phenomenon, the mesh has to be fine enough. In the results presented below, the corresponding mesh is obtained by uniformly refining the given one in Fig. 9.12b four times, in which case the total number of edges used are 623,808, the DOFs for \mathbf{E} is 621,376, and the total numbers of triangular elements and rectangular elements are 262,144 and 114,688, respectively. Hence the DOFs for H is 376,832. The time step is chosen as $\tau = 0.1$ picosecond (ps), and the total number of time steps is 50,000, i.e., $T = 5.0$ nanosecond (ns).

To see how wave propagates in the cloak structure, several snapshots of E_y fields are plotted in Fig. 9.13, which show clearly how the wave gets distorted in the cloak region. After 50,000 time steps, the plane wave pattern is almost restored, which renders the object placed inside the cloak region invisible to external electromagnetic fields.

9.4 Solar Cell Design with Metamaterials

In this section, we present an interesting application of metamaterials in solar cell design. This section is mainly derived from [192].

9.4.1 A Brief Introduction

A solar cell is a device that can directly convert solar energy into electricity through the photovoltaic effect. Generally speaking, a solar cell works in three steps: (1) Photons in sunlight hit the solar panel and are absorbed by some semiconducting materials; (2) Electrons are knocked loose from their atoms, thus forming an electric current flowing through the material; (3) An array of solar cells converts solar energy into electricity. Therefore, the operation of a solar cell requires three basic attributes: The absorption of light; The separation of various types of charge carriers; The extraction of those carriers to an external circuit.

A solar cell's performance is measured by its efficiency, which is usually broken down into reflectance efficiency, thermodynamic efficiency, charge carrier

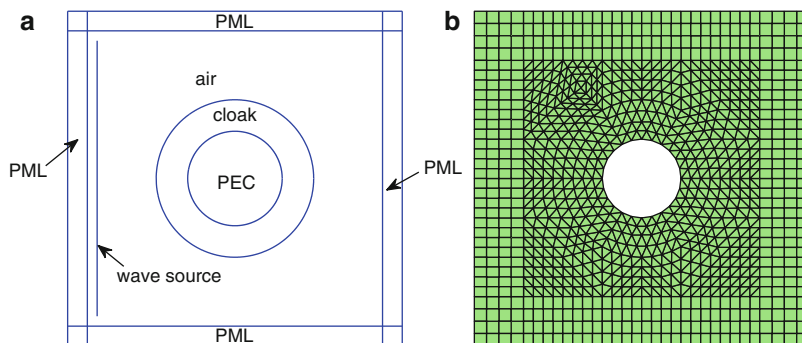


Fig. 9.12 (a) The cloak modeling setup; (b) A coarse mesh (Reprinted from Li et al. [194]. Copyright (2012), with permission from Elsevier)

separation efficiency and conductive efficiency. To reduce the cost of solar energy, high-efficiency solar cells are of interest.

Since various materials have different efficiencies and costs, creating cheap and efficient solar cells is an important research subject. Currently, many solar cells are made from bulk materials that are cut into wafers with thickness between 180–240 micrometers and are then processed like other semiconductors. The most prevalent bulk material for solar cells is crystalline silicon, which can be further classified into several categories such as monocrystalline silicon, polycrystalline silicon, and ribbon silicon.

Other solar cell materials are made as thin-film layers, organic dyes, and organic polymers. Thin-film technologies reduce the amount of materials used in solar cells. However, the majority of thin film panels have quite low conversion efficiencies and occupy large areas per watt production. Cadmium telluride, copper indium gallium selenide and amorphous silicon are three thin-film technologies often used as outdoor photovoltaic solar power production. Silicon remains the most popular material used in both bulk and thin-film forms. Silicon thin-film cells are mainly deposited by chemical vapor deposition from silane gas and hydrogen gas. Though solar cells made from various silicons such as amorphous silicon and polycrystalline silicon are cheap to produce, they still have lower energy conversion efficiency than bulk silicon.

In recent years, nanotechnology has been applied to solar cell materials, which can be made from nanocrystals and quantum dots. For example, large parallel nanowire arrays enable long absorption lengths, which can trap more light and hence improve the efficiency of the solar cell.

In the rest section we present an approach for solar cell design, which uses nanomaterials, more specifically electromagnetic metamaterials, to increase the solar cell efficiency. This approach is based on the metamaterial's striking re-focusing property (cf. Fig. 9.4 (Left)): In a planar negative-index metamaterial slab, an evanescent wave decaying away from an object grows exponentially inside

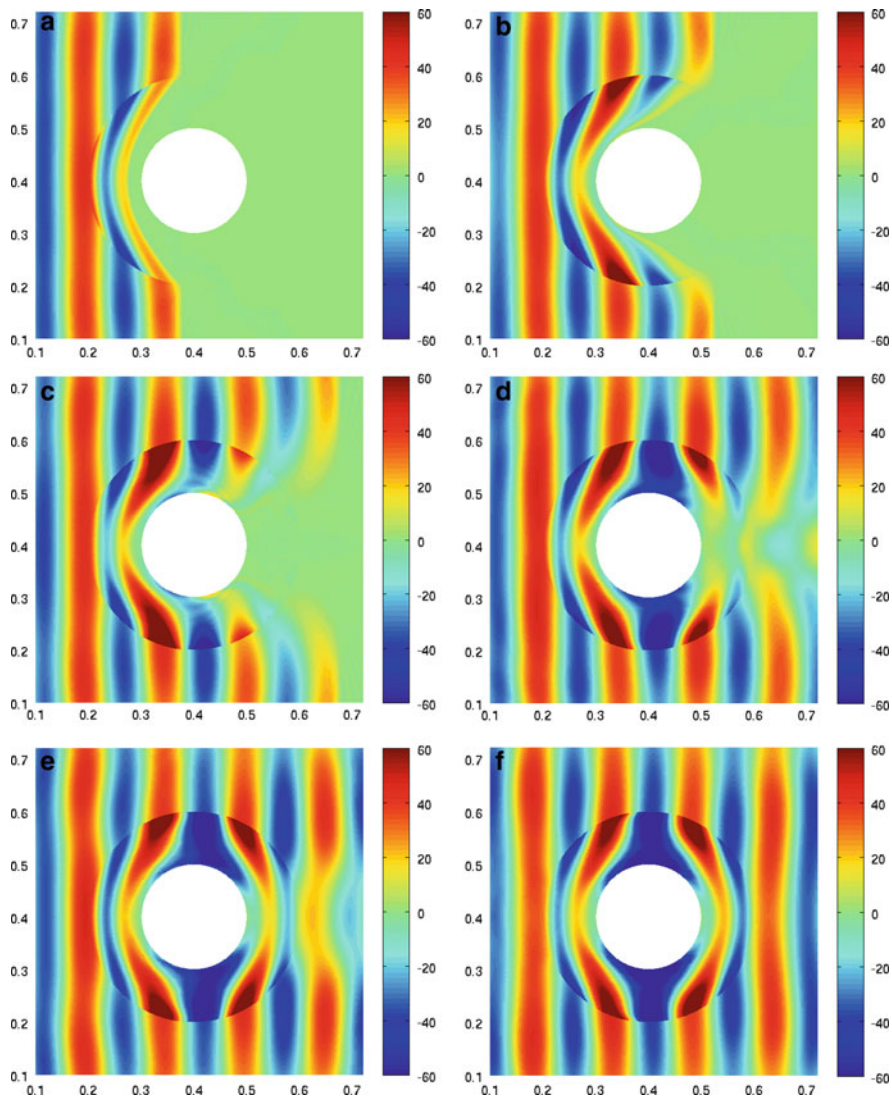


Fig. 9.13 E_y at (a) $t = 1.0$ ns; (b) $t = 1.5$ ns; (c) $t = 2.0$ ns; (d) $t = 3.0$ ns; (e) $t = 4.0$ ns; (f) $t = 5.0$ ns (Reprinted from Li et al. [194]. Copyright (2012), with permission from Elsevier)

the slab, and refocuses the source wave at the exit interface if the slab thickness equals the distance from the wave source to the slab's front interface. This property shows that metamaterials can be efficient subwavelength absorbers [14]. Ultra-thin metamaterial slabs have been shown [92] to sustain their high absorptivity for a wide range of incident angles. This property is highly desirable for developing efficient thermalphotovoltaics [175] and photovoltaics [101]. In photovoltaic applications,

the efficiency of solar cells can be enhanced by the strong field resonance inside the absorbing metamaterial.

9.4.2 The Mathematical Formulation

Modeling of solar cells boils down to solving Maxwell's equations:

$$\nabla \times \tilde{\mathbf{H}} = \frac{\partial \tilde{\mathbf{D}}}{\partial t}, \quad (9.69)$$

$$\nabla \times \tilde{\mathbf{E}} = -\frac{\partial \tilde{\mathbf{B}}}{\partial t}, \quad (9.70)$$

where $\tilde{\mathbf{E}}(\mathbf{x}, t)$ and $\tilde{\mathbf{H}}(\mathbf{x}, t)$ are the electric and magnetic fields, and $\tilde{\mathbf{D}}(\mathbf{x}, t)$ and $\tilde{\mathbf{B}}(\mathbf{x}, t)$ are the corresponding electric and magnetic flux densities. For linear electromagnetic materials, these variables are connected through the constitutive relations:

$$\tilde{\mathbf{D}} = \epsilon_0 \epsilon_r \tilde{\mathbf{E}}, \quad \tilde{\mathbf{B}} = \mu_0 \mu_r \tilde{\mathbf{H}}, \quad (9.71)$$

where ϵ_r and μ_r are the relative permittivity and permeability, respectively.

Substituting (9.71) into (9.69), (9.70), and using the time harmonic form

$$\tilde{\mathbf{E}}(\mathbf{x}, t) = \mathbf{E}(\mathbf{x})e^{j\omega t}, \quad \tilde{\mathbf{H}}(\mathbf{x}, t) = \mathbf{H}(\mathbf{x})e^{j\omega t},$$

we can transform the time-dependent Maxwell's equations into the time harmonic form:

$$j\omega\epsilon_0\epsilon_r\mathbf{E} = \nabla \times \mathbf{H}, \quad (9.72)$$

$$j\omega\mu_0\mu_r\mathbf{H} = -\nabla \times \mathbf{E}, \quad (9.73)$$

where ω denotes the wave frequency. Note that (9.72) and (9.73) can be further reduced to a simple vector wave equation in terms of either the electric field or the magnetic field:

$$\nabla \times (\mu_r^{-1} \nabla \times \mathbf{E}) - k_0^2 \epsilon_r \mathbf{E} = 0, \quad (9.74)$$

$$\nabla \times (\epsilon_r^{-1} \nabla \times \mathbf{H}) - k_0^2 \mu_r \mathbf{H} = 0. \quad (9.75)$$

Here $k_0 = \frac{\omega}{C_v} = \omega \sqrt{\epsilon_0 \mu_0}$ denotes the wave number of free space.

Under the assumption that the material is non-magnetic (hence $\mu_r = 1$), we can use the refractive index $n = \sqrt{\epsilon_r \mu_r}$ to rewrite (9.74) and (9.75) as follows:

$$\nabla \times (\nabla \times \mathbf{E}) - k_0^2 n^2 \mathbf{E} = 0, \quad (9.76)$$

$$\nabla \times (n^{-2} \nabla \times \mathbf{H}) - k_0^2 \mathbf{H} = 0. \quad (9.77)$$

To efficiently model the 2-D solar cells, we first solve (9.77) for the unknown magnetic field $H = H_z$, then postprocess H by using (9.72) to obtain the unknown electric field $\mathbf{E} = (E_x, E_y)'$, i.e.,

$$E_x = \frac{1}{j\omega\epsilon_0\epsilon_r} \frac{\partial H}{\partial y}, \quad E_y = \frac{-1}{j\omega\epsilon_0\epsilon_r} \frac{\partial H}{\partial x}.$$

9.4.3 Numerical Simulations

9.4.3.1 A Benchmark Problem

A benchmark problem of [295] is solved in [192] by using the commercial multiphysics finite element package COMSOL. The proposed solar cell structure is uniform in the z -direction. The unit cell (illustrated in Fig. 9.14) has periodic boundary conditions in the x -direction, and contains a benzocyclobutene (BCB) layer with thickness $c = 50$ nm and a gold substrate with thickness $b = 100$ nm. The gold substrate is used to absorb the radiation energy coming into the cell. Furthermore, there is a gold strip of dimension $f \times e$ embedded inside the BCB layer. In Fig. 9.14, g denotes the gap between the strip and the BCB boundary. To obtain a good absorption for the solar cell, we choose $g = 15$ nm, $f = 18$ nm, and $e = 256$ nm.

The permittivity for gold is modeled by the Drude model

$$\epsilon_r(\omega) = 1 - \frac{\omega_p^2}{\omega(\omega + i\gamma)},$$

where the plasma frequency ω_p and the collision frequency γ are calculated as

$$\gamma = \frac{\omega\epsilon_2}{1 - \epsilon_1}, \quad \omega_p = \sqrt{(1 - \epsilon_1)(\omega^2 + \gamma^2)},$$

where ϵ_1 and ϵ_2 are functions of the incident wavelength λ , obtained through polynomial fitting:

$$\begin{aligned} \epsilon_1(\lambda) &= -1.1\lambda^3 - 39\lambda^2 - 12\lambda + 12, \\ \epsilon_2(\lambda) &= 7.3\lambda^8 - 100\lambda^7 + 580\lambda^6 - 1,900\lambda^5 + 3,700\lambda^4 \\ &\quad - 4,400\lambda^3 + 3,200\lambda^2 - 1,300\lambda + 210. \end{aligned}$$

For a P-polarized radiation at frequency $2.89 \cdot 10^{14}$ Hz (which is in the infrared region) with 0° incident angle (i.e., penetrating the solar cell vertically), the obtained

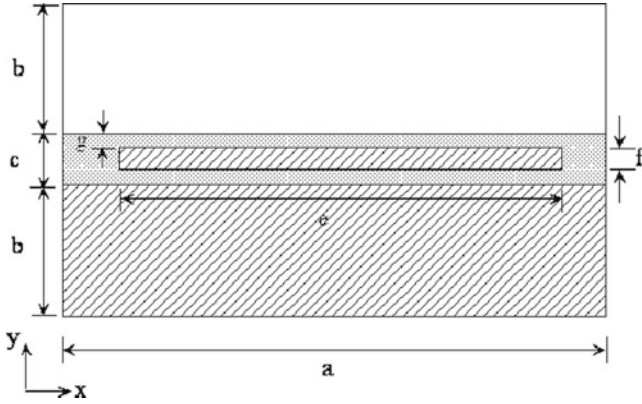


Fig. 9.14 The unit cell structure for the benchmark problem (With permission from Global Science Press [192])

electric and magnetic field magnitudes $|E_x|$, $|E_y|$ and $|H_z|$ are plotted in Fig. 9.15. In this simulation, the refractive index $n = 1.56$ is chosen for BCB, the port condition at both incident and exit surfaces is used, and Floquet periodic boundary condition is imposed in the x -direction. Furthermore, tangential continuity across subdomain interfaces is imposed.

Many numerical experiments are carried out by varying the wave incident angles and wave frequencies in the infrared (IR) and visible region. Figure 9.16 shows how the absorption varies with the incident angles in the IR and visible region. In COMSOL, the absorption on a fixed port is defined as $1 - |S_{11}|^2$, where S_{11} is the reflection coefficient expressed as

$$S_{11} = \sqrt{\text{Power reflected from the port}} / \sqrt{\text{Power incident on the port}}.$$

Furthermore, Fig. 9.16 shows that the absorption decreases as the incident angle increases for fixed frequencies, and the average absorption is about 60 % for all incident angles between 0° and 40° .

9.4.3.2 Results with Other Metals and Micro-structures

Considering the cost of gold and the uncommon BCB material, several combinations of materials were tested in [192] for their absorptions in order to find a cheap but efficient solar cell design. Detailed numerical experiments were performed with gold replaced by high melting point metals such as copper, nickel and tungsten, and with BCB replaced by dielectric SiO_2 , semiconductor C[100] and Poly-Si. Numerical results of [192] showed that the average absorption over the visible frequencies for most combinations is about 50 %.

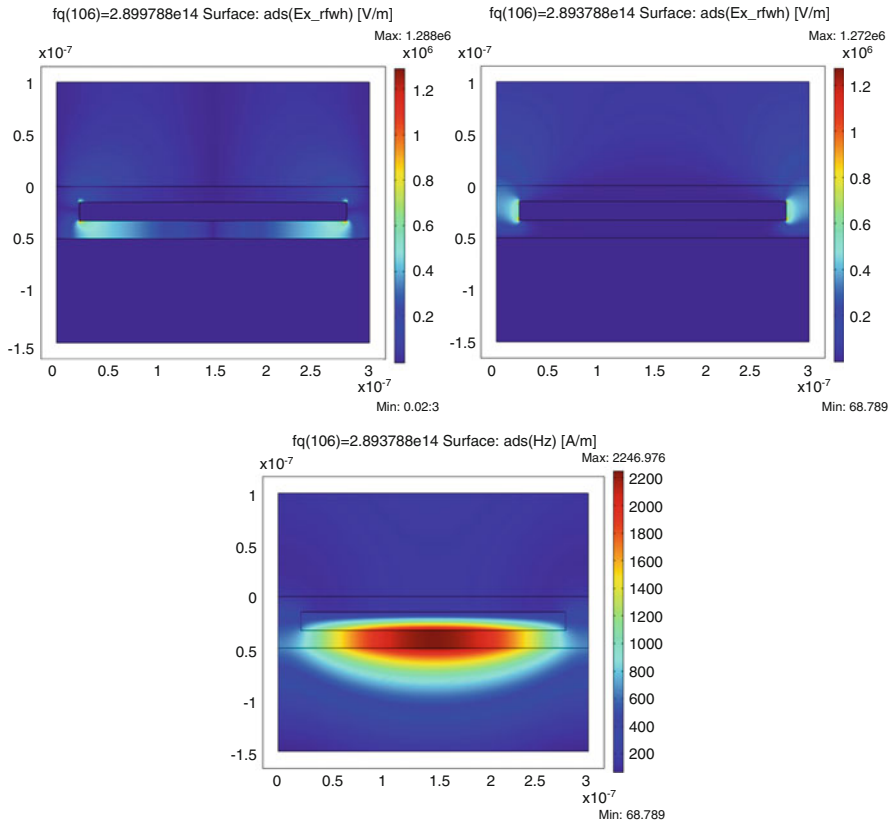


Fig. 9.15 Simulation results for the benchmark problem: (Top Right) Plot of $|E_x|$; (Top Left) Plot of $|E_y|$; (Bottom) Plot of $|H_z|$ (With permission from Global Science Press [192])

To reduce the usage of metals (hence the weight of the solar cell), [192] also considered using several micro-structures to replace the metallic strip. For example, in a nickel and Poly-Si combination, a micro-structure consisting of 44 equal rectangles with dimensions of 5 by 10 nm was tested with different frequency waves penetrating the solar cell vertically. An exemplary power flow obtained from this structure is presented in Fig. 9.17.

Another micro-structure consisting of 44 equal circles with 5 nm radius was tested for a nickel and Poly-Si combination in [192]. An exemplary power flow obtained from this micro-structure is presented in Fig. 9.18.

In [192], both the rectangular and circular micro-structures were shown to have about 80 % absorption for the vertically penetrating waves in the entire solar spectrum. Results of [192] suggest that efficient solar cells can be constructed using metamaterials.

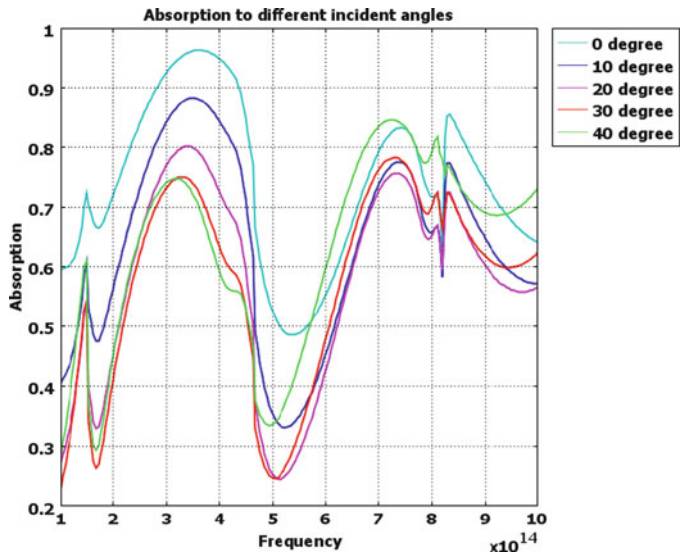


Fig. 9.16 The benchmark problem: the absorption corresponding to the infrared and visible frequencies with various incident angles (With permission from Global Science Press [192])

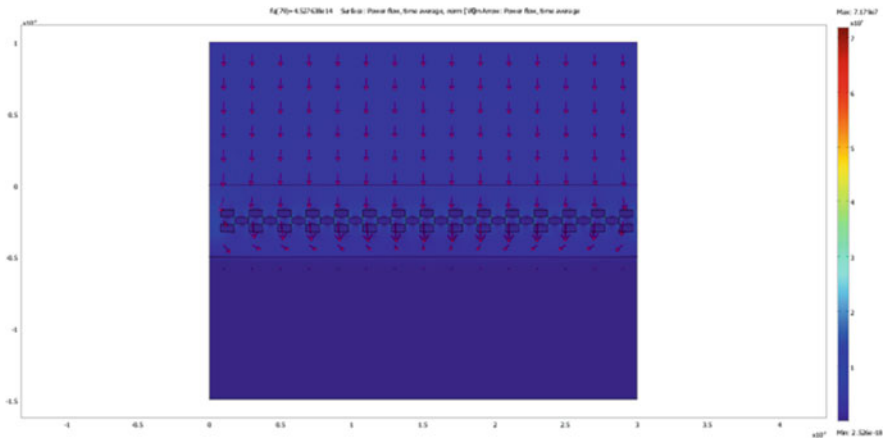


Fig. 9.17 The power flow obtained with 44 micro-rectangles (With permission from Global Science Press [192])

9.5 Problems Needing Special Attention

9.5.1 Unit Cell Design and Homogenization

The metamaterials discussed in this book are structured composites which lead to simultaneously negative permittivity and permeability. A key issue in the theory of composites [211] is the study of how their physical properties such as permittivity

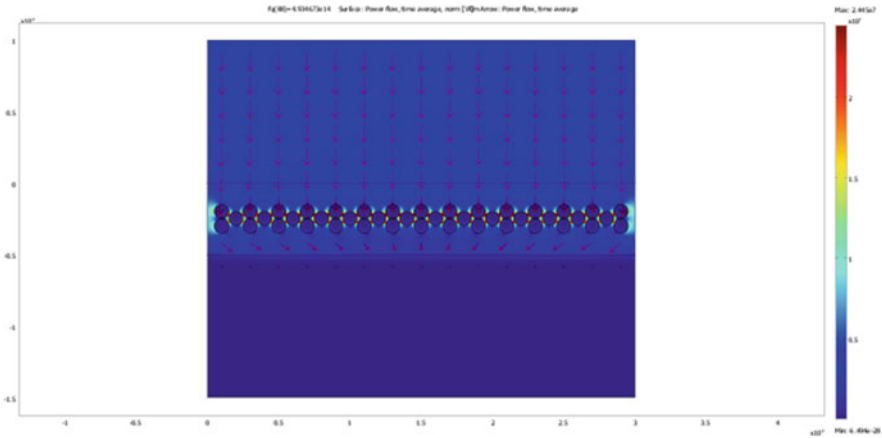


Fig. 9.18 The power flow obtained with 44 micro-circles (With permission from Global Science Press [192])

and permeability depend on the microstructure (or unit cell). When the period of the microstructure is small compared to the wavelength, the physical parameters in Maxwell's equations oscillate rapidly, which makes the numerical simulation very challenging. In this case, homogenization approach [33, 81, 250] is often used: the rapidly oscillating parameters are replaced with effective constitutive parameters. A distinguishing feature of the homogenization problem for metamaterials is that the cell size a is not vanishingly small compared to the vacuum wavelength λ_0 at a given frequency. The typical range in practice is $a \sim 0.1 - 0.3\lambda_0$. Hence, the classical homogenization procedures valid for $a \rightarrow 0$ have limited applicability for metamaterials. In the physics and engineering community, the homogenized material parameters are often calculated using S-parameter retrieval method [71, 196], the field-averaging method [270], and other averaging operations such as Maxwell-Garnett, Bruggeman and Clausius-Mossotti mixing formulas (cf. [264] and references cited therein). Rigorous mathematical treatment of the homogenization of metamaterials is still in its early stages [27, 47, 165, 231], and much more work is needed in this direction.

In the mathematics community, there are already many studies devoted to homogenization of Maxwell's equations. It is well known that homogenization results can be obtained by the classical method of asymptotic expansions in two scales for Maxwell's equations (see e.g. [33, 250]). Homogenization for the non-stationary Maxwell's system is discussed in books [161, 250]. Using the two-scale convergence method, Wellander [291] obtained convergence results for the homogenization method for the time-dependent Maxwell's equations in a heterogeneous medium obeying linear constitutive relations. Barbatis and Stratis [27] studied the periodic homogenization of Maxwell's equations for dissipative bianisotropic media in the time domain. Using the periodic unfolding method (originally introduced by Cioranescu et al. [80] in the abstract framework of elliptic equations), Bossavit,

Griso, and Miara [46] investigated the behavior of the electromagnetic field of a medium with periodic microstructures made of bianisotropic material and proved convergence results for their homogenization method. In 2006, Banks et al. [24] used the periodic unfolding method and derived homogenization results of the nonstationary Maxwell's equations in dispersive media. On the other hand, there are many more homogenization publications for time-harmonic Maxwell's equations than the time-dependent Maxwell's equations (see e.g. [60, 169, 268] and references therein).

To bring interested readers to the forefront of homogenization, below we present two examples of homogenization of time-dependent Maxwell's equations in composite materials with periodic microstructures in 3-D. The first example is for Maxwell's equations written in one vector wave equation. The second example is for Maxwell's equations expressed as a system of first-order differential equations.

9.5.1.1 Homogenization via Multiscale Asymptotic Expansion

Consider the time-dependent Maxwell's equations with rapidly oscillatory coefficients as follows:

$$\frac{\partial^2 \mathbf{u}^\alpha(x, t)}{\partial t^2} + \operatorname{curl}(A(\frac{x}{\alpha}) \operatorname{curl} \mathbf{u}^\alpha(x, t)) = \mathbf{f}(x, t), \quad \text{in } \Omega \times (0, T), \quad (9.78)$$

$$\nabla \cdot \mathbf{u}^\alpha = 0, \quad \text{in } \Omega \times (0, T), \quad (9.79)$$

$$\mathbf{n} \times \mathbf{u}^\alpha(x, t) = 0, \quad \text{on } \partial\Omega \times (0, T), \quad (9.80)$$

$$\mathbf{u}^\alpha(x, 0) = \mathbf{u}_0(x), \quad \partial_t \mathbf{u}^\alpha(x, 0) = \mathbf{u}_1(x), \quad \text{in } \Omega, \quad (9.81)$$

where \mathbf{u} can be either the electric field \mathbf{E} or magnetic field \mathbf{H} , and the matrix function $A(\frac{x}{\alpha}) = (a_{ij}(\frac{x}{\alpha})), i, j = 1, 2, 3$. Here the small number $\alpha > 0$ represents the size of the periodic microstructure of a composite material (see Fig. 9.19).

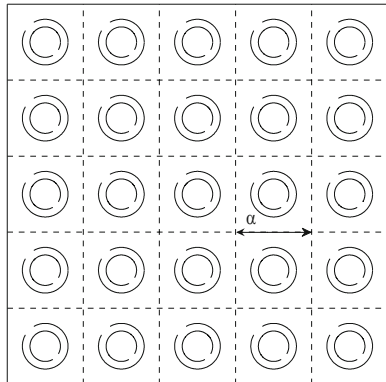
Note that when α becomes quite small, direct accurate numerical computation of the solution \mathbf{u}^α is very challenging or even impossible since a very fine mesh is required which leads to a prohibitive amount of memory storage and computational time. For clarity, we denote $\xi = \frac{x}{\alpha}$. In the classic multiscale asymptotic method, x and ξ are called “slow” and “fast” variables, respectively. Furthermore, we denote $Q = (0, 1)^3$ for the reference cell of the periodic structure. The remaining material of this subsection is essentially from [33, Sect. 11 of Chap. 1] and [60, 302].

The solution \mathbf{u}^α to the problem (9.78)–(9.81) can be approximated by the two-scale asymptotic expansion

$$\mathbf{u}^\alpha(x, t) = \mathbf{u}^*(x, t) + \alpha \theta_1(\xi) \operatorname{curl} \mathbf{u}^*(x, t) + \alpha^2 \theta_2(\xi) \operatorname{curl}^2 \mathbf{u}^*(x, t) + \cdots, \quad (9.82)$$

where $\operatorname{curl}^2 = \operatorname{curl} \operatorname{curl}$, \mathbf{u}^* is the solution to a homogenized problem, and $\theta_1(\xi)$ and $\theta_2(\xi)$ are corrector functions. Details are given below.

Fig. 9.19 A composite material with periodic microstructures



Substituting (9.82) into (9.78), using the fact that $\text{curl} = \text{curl}_x + \text{curl}_\xi$, and equalizing all terms with power α^{-1} , we have: for $k = 1, 2, 3$,

$$\text{curl}_\xi(A(\xi)\text{curl}_\xi\theta_1^k(\xi) + A(\xi)e_k) = 0, \quad \text{in } Q, \quad (9.83)$$

$$\nabla_\xi \cdot \theta_1^k(\xi) = 0, \quad \text{in } Q, \quad (9.84)$$

$$\mathbf{n} \times \theta_1^k(\xi) = 0, \quad \text{on } \partial Q, \quad (9.85)$$

where e_k is the canonical basis of R^3 . Using $\theta_1^k(\xi)$, we can form the matrix cell function $\theta_1(\xi) = (\theta_1^1(\xi), \theta_1^2(\xi), \theta_1^3(\xi))$.

Similarly, equalizing the terms with power α^0 , we can define $\tilde{\theta}_2^k(\xi)$, $k = 1, 2, 3$, which satisfy

$$\text{curl}_\xi(A(\xi)\text{curl}_\xi\tilde{\theta}_2^k(\xi)) = -\text{curl}_\xi(A(\xi)\theta_1^k(\xi)) + G(\xi), \quad \text{in } Q, \quad (9.86)$$

$$\mathbf{n} \times \tilde{\theta}_2^k(\xi) = 0, \quad \text{on } \partial Q, \quad (9.87)$$

where $G(\xi) = -A(\xi)\text{curl}_\xi\theta_1^k(\xi) - A(\xi)e_k + A^*e_k$, and A^* is the homogenized coefficient matrix defined as (cf. (11.44) of [33, p. 145])

$$A^* = \int_Q (A(\xi) + A(\xi)\text{curl}_\xi\theta_1(\xi))d\xi. \quad (9.88)$$

Note that if $\nabla_\xi \cdot G(\xi) \neq 0$, then no solution exists for Eq. (9.86). To avoid this issue, we can introduce scalar functions $\phi^k(\xi)$, $k = 1, 2, 3$, which satisfy

$$-\Delta_\xi\phi^k(\xi) = \nabla_\xi \cdot G(\xi) \quad \text{in } Q, \quad (9.89)$$

$$\phi^k(\xi) = 0, \quad \text{on } \partial Q. \quad (9.90)$$

Now we can define $\theta_2^k(\xi)$, $k = 1, 2, 3$ such that

$$\begin{aligned} & \operatorname{curl}_\xi(A(\xi)\operatorname{curl}_\xi\theta_2^k(\xi)) \\ &= -\operatorname{curl}_\xi(A(\xi)\theta_1^k(\xi)) + G(\xi) + \nabla_\xi\phi^k(\xi), \quad \text{in } Q, \end{aligned} \quad (9.91)$$

$$\nabla_\xi \cdot \theta_2^k(\xi) = 0, \quad \text{in } Q, \quad (9.92)$$

$$\mathbf{n} \times \theta_2^k(\xi) = 0, \quad \text{on } \partial Q, \quad (9.93)$$

from which we construct the matrix cell function $\theta_2(\xi) = (\theta_2^1(\xi), \theta_2^2(\xi), \theta_2^3(\xi))$.

It is shown [302] that $\mathbf{u}^*(x, t)$ is the solution to the following homogenized Maxwell's equations:

$$\frac{\partial^2 \mathbf{u}^*(x, t)}{\partial t^2} + \operatorname{curl}(A^* \operatorname{curl} \mathbf{u}^*(x, t)) = \mathbf{f}(x, t), \quad \text{in } \Omega \times (0, T), \quad (9.94)$$

$$\nabla \cdot \mathbf{u}^* = 0, \quad \text{in } \Omega \times (0, T), \quad (9.95)$$

$$\mathbf{n} \times \mathbf{u}^*(x, t) = 0, \quad \text{on } \partial\Omega \times (0, T), \quad (9.96)$$

$$\mathbf{u}^*(x, 0) = \mathbf{u}_0(x), \quad \partial_t \mathbf{u}^*(x, 0) = \mathbf{u}_1(x), \quad \text{in } \Omega. \quad (9.97)$$

It is proved [250] that if $A(\xi)$ is symmetric and positive definite, and elements $a_{ij}(\xi)$ are 1-periodic in ξ , then the problem (9.78)–(9.81) has a unique solution $\mathbf{u}^\alpha(x, t) \in L^2(0, T; H(\operatorname{curl}; \Omega)) \cap C^0(0, T; (L^2(\Omega))^3)$ under the assumption that $\mathbf{f} \in L^2(0, T; (L^2(\Omega))^3)$, $\mathbf{u}_0 \in (H^1(\Omega))^3$, $\mathbf{u}_1 \in (L^2(\Omega))^3$. Furthermore,

$$\mathbf{u}^\alpha(x, t) \rightarrow \mathbf{u}^*(x, t) \quad \text{in } L^\infty(0, T; (L^2(\Omega))^3) \text{ weakly } \star.$$

Under more regularity assumptions, Zhang et al. [302] proved that the two-scale asymptotic expansions for problem (9.78)–(9.81):

$$\mathbf{u}_1^\alpha(x, t) = \mathbf{u}^*(x, t) + \alpha\theta_1(\xi)\operatorname{curl} \mathbf{u}^*(x, t)$$

and

$$\mathbf{u}_2^\alpha(x, t) = \mathbf{u}^*(x, t) + \alpha\theta_1(\xi)\operatorname{curl} \mathbf{u}^*(x, t) + \alpha^2\theta_2(\xi)\operatorname{curl}^2 \mathbf{u}^*(x, t)$$

converges to $\mathbf{u}^\alpha(x, t)$ uniformly in α . More specifically, they proved

$$\|\mathbf{u}^\alpha(x, t) - \mathbf{u}_k^\alpha(x, t)\|_{L^\infty(0, T; H(\operatorname{curl}; \Omega))} + \|\partial_t(\mathbf{u}^\alpha(x, t) - \mathbf{u}_k^\alpha(x, t))\|_{L^\infty(0, T; (L^2(\Omega))^3)} \leq C\alpha$$

for $k = 1, 2$. Here C is a constant independent of the small structure size α .

Finally, we like to remark that the homogenized problem (9.94)–(9.97) is a Maxwell system with constant coefficients, and it can be solved by various numerical methods on a relatively coarse mesh. Furthermore, the corrector functions

$\theta_1(\xi)$ and $\theta_2(\xi)$ need to be solved on a unit cell only once. Hence an efficient multiscale finite element method can be developed for Maxwell's equations with rapidly oscillatory coefficients. For details, see [60, 302].

9.5.1.2 Homogenization by the Periodic Unfolding Method

The periodic unfolding method was introduced by Cioranescu et al. [80] in the abstract framework of elliptic equations, and later were extended to Maxwell's equations used for simulating the electromagnetic field in composite media with spatially periodic microstructures [24, 46], from which this subsection is mainly derived.

Consider the Maxwell's equations posted on $\Omega \times (0, T)$:

$$\frac{\partial \mathbf{D}(x, t)}{\partial t} = \text{curl } \mathbf{H}(x, t) - \mathbf{J}_s(x, t), \quad (9.98)$$

$$\frac{\partial \mathbf{B}(x, t)}{\partial t} = -\text{curl } \mathbf{E}(x, t), \quad (9.99)$$

with initial conditions

$$\mathbf{E}(x, 0) = \mathbf{E}_0(x), \quad \mathbf{H}(x, 0) = \mathbf{H}_0(x),$$

and the perfect conducting boundary condition

$$\mathbf{n} \times \mathbf{E} = 0 \quad \text{on } \partial\Omega \times (0, T).$$

This system is completed by the general constitutive laws

$$\mathbf{D}(x, t) = \epsilon_0 \epsilon_r(x) \mathbf{E}(x, t) + \int_0^t \{\sigma_E(x) + \nu_E(x, t-s)\} \mathbf{E}(x, s) ds, \quad (9.100)$$

$$\mathbf{B}(x, t) = \mu_0 \mu_r(x) \mathbf{H}(x, t) + \int_0^t \{\sigma_H(x) + \nu_H(x, t-s)\} \mathbf{H}(x, s) ds, \quad (9.101)$$

where ϵ_0 and μ_0 are the permittivity and permeability of free space, ϵ_r and μ_r are the relative permittivity and permeability of the media, σ_E and σ_H are the electric and magnetic conductivities, μ_E and μ_H are the electric and magnetic susceptibilities, and \mathbf{J}_s is the source current density.

Let us introduce the vector of fields

$$\mathbf{u} = \begin{pmatrix} \mathbf{E} \\ \mathbf{H} \end{pmatrix} \in W^{1,1}(0, T; H^1(\Omega; \mathbb{R}^6)), \quad (9.102)$$

and the operator

$$L\mathbf{u}(x, t) = \begin{pmatrix} \mathbf{D}(x, t) \\ \mathbf{B}(x, t) \end{pmatrix}, \quad (9.103)$$

which can be written as

$$L\mathbf{u}(x, t) = A(x)\mathbf{u}(x, t) + \int_0^t \{F(x) + G(x, t-s)\}\mathbf{u}(x, s)ds, \quad (9.104)$$

where the 6×6 matrices A , F and G are defined as

$$A(x) = \begin{pmatrix} \epsilon_0 \epsilon_r(x) I_3 & 0_3 \\ 0_3 & \mu_0 \mu_r(x) I_3 \end{pmatrix}, \quad F(x) = \begin{pmatrix} \sigma_E I_3 & 0_3 \\ 0_3 & \sigma_H I_3 \end{pmatrix}, \quad (9.105)$$

$$G(x, t) = \begin{pmatrix} \nu_E(x, t) I_3 & 0_3 \\ 0_3 & \nu_H(x, t) I_3 \end{pmatrix}. \quad (9.106)$$

Here I_3 and 0_3 denote the 3×3 identity and zero matrices, respectively.

Furthermore, we define the Maxwell operator M as

$$M\mathbf{u}(x, t) = M \begin{pmatrix} \mathbf{E} \\ \mathbf{H} \end{pmatrix} = \begin{pmatrix} \text{curl } \mathbf{H}(x, t) \\ -\text{curl } \mathbf{E}(x, t) \end{pmatrix} \quad (9.107)$$

and the vector $\mathbf{J}_s(t) = (\mathbf{J}_s(t), 0, 0, 0) \in R^6$. Hence we can rewrite the Maxwell's equations in the form

$$\frac{d}{dt} L\mathbf{u} = M\mathbf{u} - \mathbf{J}_s(t), \quad \text{in } \Omega \times (0, T), \quad (9.108)$$

$$\mathbf{u}(x, 0) = \mathbf{u}^0(x), \quad \text{in } \Omega, \quad (9.109)$$

$$\mathbf{n} \times \mathbf{u}_1(x, t) = 0, \quad \text{on } \partial\Omega \times (0, T), \quad (9.110)$$

where $\mathbf{u}_1 = \mathbf{E}$.

Now we assume that the medium occupying the domain Ω has periodic microstructures, i.e., $\epsilon_r, \mu_r, \sigma_E, \sigma_H, \nu_E$ and ν_H are highly oscillatory functions in space, which lead to matrices A , F and G with spatially oscillatory coefficients. In this case, we have to solve the following Maxwell's equations:

$$\begin{aligned} \frac{d}{dt} (A^\alpha(x) \mathbf{u}^\alpha(x, t) + \int_0^t \{F^\alpha(x) + G^\alpha(x, t-s)\} \mathbf{u}^\alpha(x, s) ds) \\ = M\mathbf{u}^\alpha - \mathbf{J}_s(t), \quad \text{in } \Omega \times (0, T), \end{aligned} \quad (9.111)$$

$$\mathbf{u}^\alpha(x, 0) = \mathbf{u}^0(x), \quad \text{in } \Omega, \quad (9.112)$$

$$\mathbf{n} \times \mathbf{u}_1^\alpha(x, t) = 0, \quad \text{on } \partial\Omega \times (0, T), \quad (9.113)$$

where we assume that the periodic structure is characterized by an elementary microstructure with size $\alpha > 0$, i.e., we assume that

$$A^\alpha(x) = A(x, \frac{x}{\alpha}), \quad F^\alpha(x) = F(x, \frac{x}{\alpha}), \quad G^\alpha(x) = G(x, \frac{x}{\alpha}).$$

We approximate the solution \mathbf{u}^α of (9.111)–(9.113) by the two-scale expansion

$$\mathbf{u}^\alpha(x, t) = \mathbf{u}^*(x) + \nabla_\xi \bar{\mathbf{u}}(x, \xi) + \cdots, \quad x \in \Omega, \quad \xi \in Q, \quad (9.114)$$

where \mathbf{u}^* is a solution to the homogenized problem (9.115) and (9.116) shown below, and $\bar{\mathbf{u}}$ is the first corrector term. Recall that Q denotes the reference cell $(0, 1)^3$. Before we present the specific form of the homogenized problem, we have to introduce some corrector functions first.

Let us denote $H_{per}^1(Q)$ for the space of periodic functions with vanishing mean value. By Bossavit et al. [46, p. 848], corrector functions $\bar{w}_k^A \in H_{per}^1(Q; R^2)$, $\bar{w}_k \in W^{1,1}(0, T; H_{per}^1(Q; R^2))$ and $\bar{w}_k^0 \in W^{2,1}(0, T; H_{per}^1(Q; R^2))$ are solutions to the following variational problems:

$$\begin{aligned} (i) \quad & \int_Q A(\xi) \nabla_\xi \bar{w}_k^A \cdot \nabla_\xi \bar{v}(\xi) d\xi = - \int_Q A(\xi) e_k \cdot \nabla_\xi \bar{v}(\xi) d\xi, \\ (ii) \quad & \int_Q \{A(\xi) \nabla_\xi \bar{w}_k(\xi, t) + \int_0^t (F(\xi) + G(\xi, t-s)) \nabla_\xi \bar{w}_k(\xi, s) ds\} \cdot \nabla_\xi \bar{v}(\xi) d\xi \\ & = - \int_Q (F(\xi) + G(\xi, t)) (e_k + \nabla_\xi \bar{w}_k^A) \cdot \nabla_\xi \bar{v}(\xi) d\xi, \\ (iii) \quad & \int_Q \{A(\xi) \nabla_\xi \bar{w}_k^0(\xi, t) + \int_0^t (F(\xi) + G(\xi, t-s)) \nabla_\xi \bar{w}_k^0(\xi, s) ds\} \cdot \nabla_\xi \bar{v}(\xi) d\xi \\ & = - \int_Q A(\xi) e_k \cdot \nabla_\xi \bar{v}(\xi) d\xi, \end{aligned}$$

for all $\bar{v} \in H_{per}^1(Q; R^2)$ and $k = 1, 2, \dots, 6$. Here the vector e_k is the canonical basis of R^6 , and ∇_ξ is the divergence operator defined as $\nabla_\xi = (\nabla_{\xi_1}, \nabla_{\xi_2}, \nabla_{\xi_3})' \in R^{3 \times 1}$. For a vector $\mathbf{v} = (v_1, v_2)'$, where v_1 and v_2 are scalar functions, we define $\nabla_\xi \mathbf{v} = (\nabla_{\xi_1} v_1, \nabla_{\xi_2} v_2)' \in R^{6 \times 1}$.

It is proved [46] that \mathbf{u}^* is the solution to the homogenized problem:

$$\frac{d}{dt} L^* \mathbf{u} = M \mathbf{u} - \mathbf{J}_s - \mathbf{J}^0, \quad \text{in } \Omega \times (0, T), \quad (9.115)$$

$$\mathbf{u}(x, 0) = \mathbf{u}^0(x), \quad \text{in } \Omega, \quad (9.116)$$

$$\mathbf{n} \times \mathbf{u}_1(x, t) = 0, \quad \text{on } \partial\Omega \times (0, T), \quad (9.117)$$

where the operator L^* is defined as

$$L^* \mathbf{u}(x, t) = A^* \mathbf{u}(x, t) + \int_0^t \{F^* + G^*(t-s)\} \mathbf{u}(x, s) ds, \quad (9.118)$$

where the homogenized 6×6 matrices A^* , F^* and G^* are computed as follows:

$$A_k^* = \int_Q A(\xi) \{e_k + \nabla_\xi \bar{w}_k^A(\xi)\} d\xi, \quad (9.119)$$

$$F_k^* = \int_Q F(\xi) \{e_k + \nabla_\xi \bar{w}_k^A(\xi)\} d\xi, \quad (9.120)$$

$$\begin{aligned} G_k^*(t) &= \int_Q G(\xi, t) \{e_k + \nabla_\xi \bar{w}_k^A(\xi)\} d\xi + \int_Q A(\xi) \nabla_\xi \bar{w}_k(\xi, t) d\xi \\ &\quad + \int_Q \int_0^t \{F(\xi) + G(\xi, t-s)\} \nabla_\xi \bar{w}_k(\xi, s) ds d\xi, \end{aligned} \quad (9.121)$$

for $k = 1, 2, \dots, 6$, and A_k^* , F_k^* and G_k^* are the column vectors of A^* , F^* and G^* .

The extra source term \mathbf{J}^0 in (9.115) is given by

$$J_k^0(x, t) = u_k^0(x) \frac{d}{dt} \left\{ \int_Q (A \nabla_\xi \bar{w}_k^0(t) + \int_0^t (F + G(t-s)) \nabla_\xi \bar{w}_k^0(s) ds) d\xi \right\}, \quad (9.122)$$

for $k = 1, 2, \dots, 6$. Here $u_k^0(x)$ are components of the decomposition $\mathbf{u}^0(x) = u_k^0(x) e_k$.

Similarly, by considering the decomposition $\mathbf{u}^*(x, t) = u_k^*(x, t) e_k$, we can obtain the corrector $\bar{\mathbf{u}} \in W^{2,1}(0, T; H_{per}^1(Q; R^2))$ as

$$\bar{\mathbf{u}}(x, \xi, t) = \bar{w}_k^A(\xi) u_k^*(x, t) + \int_0^t \bar{w}_k(\xi, t-s) u_k^*(x, s) ds + \bar{w}_k^0(\xi, t) u_k^0(x), \quad (9.123)$$

or in matrix form:

$$\bar{\mathbf{u}}(x, \xi, t) = \bar{w}^A(\xi) \mathbf{u}^*(x, t) + \int_0^t \bar{w}(\xi, t-s) \mathbf{u}^*(x, s) ds + \bar{w}^0(\xi, t) \mathbf{u}^0(x),$$

where $\bar{w}^A \in R^{2 \times 6}$ with columns \bar{w}_k^A , $k = 1, 2, \dots, 6$. Similarly, \bar{w}^0 and $\bar{w} \in R^{2 \times 6}$.

By solving corrector variational problems and the homogenized problem (9.115)–(9.117) using finite element methods on a regular mesh, we can obtain a quite accurate numerical solution to the original rapidly oscillatory coefficient problem (9.111)–(9.113).

9.5.2 *A Posteriori Error Estimator*

Due to the pioneering work of Babuska and Rheinboldt in the late 1970s [16], the adaptive finite element method has been well developed as evidenced by the vast literature in this area (cf. review papers [32, 64, 111, 126, 227], books [4, 20, 21, 252, 287, 297], and references cited therein). One important task in adaptive finite element method is to develop a robust and effective a posteriori error estimator, which can be used to guide where to refine or coarsen the mesh and/or how to choose the proper orders of the basis functions in different regions. As we mentioned in Sect. 6.1, though the study of a posteriori error estimator for elliptic, parabolic and second order hyperbolic problems seems mature, publications on a posteriori error estimator for Maxwell's equations are quite limited and are almost exclusively for the lowest-order edge element used for the model problem:

$$\nabla \times (\alpha \nabla \times \mathbf{u}) + \beta \mathbf{u} = \mathbf{f} \text{ in } \Omega \subset R^3, \text{ and } \mathbf{n} \times \mathbf{u} = \mathbf{0} \text{ on } \Gamma. \quad (9.124)$$

In 2009, Li [182] initiated analysis of a posteriori error estimator for time-dependent Maxwell's equations when cold plasma is involved. However, results of [182] are only for a semi-discrete scheme (cf. Sect. 6.3). Much more work is needed for edge elements with applications to Maxwell's equations when complex media such as metamaterials are involved.

Another area worth exploring is the hp-adaptive method [17, 97, 98, 255] by varying both the mesh sizes and the orders of the basis functions. It is known that some pioneering works on hp methods have been initiated for time-harmonic Maxwell's equations (e.g., [3, 97, 98, 273] and references cited therein). Extending them to time-domain Maxwell's equations involving metamaterials would be interesting but very challenging. Even for the free space case, the application of *hp* $H(\text{curl})$ conforming finite element method to time-domain computational electromagnetics remain in its infancy [176, p. 295]. Furthermore, from a theoretical point of view, the hp finite element analysis for Maxwell's equations has just started (e.g. [91, p. 578] and [238]).

9.5.3 *Concluding Remarks*

The amount of literature and topics on metamaterials are so vast that our bibliography is by no means exhaustive. For example, there are increasingly more works on acoustic and elastic metamaterials, and acoustic and elastic cloaking (e.g., [143, 214, 229, 233]). We decided to skip these subjects, since the underlying equations are totally different from the time-domain Maxwell's equations we focused on. Interested readers can refer to a very recent book edited by Craster and Guenneau [93], which is dedicated to this subject. We hope that the selected entries provide readers with a way to examine the covered topics more deeply.

Due to our limited experience in applications of metamaterials, we feel very sorry for missing any engineering and physics references. Readers can consult those published metamaterial books mentioned in Chap. 1.

Even from a mathematical modeling and scientific computing viewpoint, our book provides only an introduction to modeling wave propagation in metamaterials by using the so-called time-domain finite element methods. More robust and efficient numerical methods should be investigated in the future. To inspire more computational scientists (especially young researchers) to enter into this exciting area, below we summarize a list of interesting topics (at least to us) to be explored:

1. *Well-posedness and regularity* Though we investigated the well-posedness of some Maxwell's equations resulting from those popular metamaterial models, there are other models we haven't looked into yet. An important and challenging issue is how regular the solutions can be, since singularities can be caused by many things such as non-trivial physical domains, discontinuous material coefficients, and non-smooth source terms. Even for Maxwell's equations in free space, the analysis is quite involved (e.g., [89, 90]).
2. *Mass-lumping* For time-dependent large-scale simulations, it seems that explicit schemes such as leap-frog types are quite popular. However, inverting a mass matrix makes the algorithm not fully explicit. One way to overcome this issue is the so-called mass-lumping technique, which approximates the mass matrix by a diagonal matrix to speed up the simulation. Though some strategies have been proposed [86, 87, 108, 121], some issues remain to be resolved such as how to do mass-lumping for high-order edge elements, how to do mass-lumping on hybrid grids, and how mass-lumping affects the accuracy and dispersion error etc.
3. *Dispersion and dissipation analysis* The dispersive and dissipative errors play a very important role in wave propagation modeling. Though dispersion analysis has been carried out for Maxwell's equations in free space [87, 218, 279] and in dispersive media [25], no such analysis has been carried out for Maxwell's equations in metamaterials.
4. *Multiscale techniques* Since metamaterials are composites of periodic microstructures, it would be beneficial to develop some numerical methods coupled with multiscale techniques [105, 110, 293]. Some homogenization works on metamaterials have been carried out (e.g. [27, 47, 165, 231]), and much more work is needed in this direction.
5. *Nonconforming elements* Recent works [52, 103, 150, 242] show that it is possible to design convergent nonconforming finite element methods for solving time-harmonic Maxwell equations. Some comparisons with edge elements would be great, and applications of those nonconforming elements should be carried out to see if they can correctly simulate the wave propagation phenomena in metamaterials.
6. *Fast solvers* To improve the efficiency and robustness of linear system solvers, multigrid methods [136, 300] and domain decomposition methods [280] have been intensively investigated over the past three decades. Though there are

many publications on these subjects for edge elements used for time-harmonic Maxwell's equations (e.g. [5, 12, 129, 144, 146, 149, 281, 307]), very few papers exist for metamaterial Maxwell's equations. Recently, the so-called sweeping preconditioners proposed in [283] seem very efficient in solving time-harmonic Maxwell's equations with edge elements. Their numerical results with unstructured meshes (including a cloaking example) have demonstrated $O(N)$ complexity in 2-D and $O(N \log N)$ complexity in 3-D. It would be interesting to see how this algorithm performs for high order edge elements and time dependent problems.

7. *A posteriori error estimation* A posteriori error estimation plays a very important role in adaptive finite element methods. There is a huge amount of literature on a posteriori error estimation (cf. [4, 20, 21, 252, 287, 297] and references cited therein). As we mentioned in Chap. 6, there are no more than 20 papers on a posteriori error estimation based on edge elements for Maxwell's equations. Additionally, most works are mainly on the lowest-order edge elements and just for Maxwell's equations in free space. Hence there is a great opportunity to obtain many interesting results for metamaterial models.
8. *Superconvergence* As mentioned in Chap. 5, many interesting results have been obtained for standard equations such as elliptic, parabolic and the second-order hyperbolic types (cf. [67, 201, 289]). But superconvergence results on edge elements for solving Maxwell's equations (especially when metamaterials are involved) are quite limited. So far, superconvergence has been proved and demonstrated for bilinear or trilinear edge elements [153, 198, 202, 215], and the lowest-order triangular edge elements formed as pairs of parallelograms [154]. It is still unknown whether superconvergence exists for tetrahedral edge elements, or even higher-order triangular edge elements.
9. *H_p-adaptivity* The *hp*-adaptive finite element method can be thought as the most desirable method in that the mesh size and basis function order can be automatically adapted during a computer simulation. In this sense, adaptive DG methods can be put into the *hp* method family. It is known that the realization of an efficient *hp* method is very challenging. As we mentioned in Sect. 9.5.2, the *hp* finite element analysis and application for time-dependent Maxwell's equations still has many issues to be resolved.
10. *Frequency-domain analysis* In the book, we mainly focused on time-domain simulation of Maxwell's equations in metamaterials. It would be interesting to consider the metamaterial simulation in frequency-domain. Though many applications of frequency-domain finite element (FEFD) methods have been carried out by engineers, numerical analysis of FEFD methods seems quite limited (cf. Fernandes and Raffetto's works [117–119], and Bonnet-Ben Dhia et al. [43, 44]). Further exploration in this direction should be done in the future.